Petroleum Science 23 (2026) 1606–1623

Contents lists available at ScienceDirect

Petroleum Science

journal homepage: www.keaipublishing.com/en/journals/petroleum-science

Original Paper

Feasibility of underground gas storage construction from large-scale low-permeability lithologic gas reservoirs: Insights into microscopic storage spaces

Zhen-Hua Tian [a,b,*], Yong Xia [a,b], Jian-Guo Zhang [a,b], De-Long Wang [a,b], Zhi-Jun Liu [a,b], Chen-Yang Zhao [a,b], Yu-Xuan Xia [c], Jun-Wei Su [d], Deng-Ke Liu [d], Jian-Chao Cai [c,**]

[a] Research Institute of Exploration and Development, PetroChina Changqing Oilfield Company, Xi'an, 710018, Shaanxi, China
[b] National Engineering Laboratory for Exploration and Development of Low-permeability Oil & Gas Fields, Xi'an, 710018, Shaanxi, China
[c] State Key Laboratory of Petroleum Resources and Engineering, China University of Petroleum (Beijing), Beijing, 102249, China
[d] School of Human Settlement and Civil Engineering, Xi'an Jiaotong University, Xi'an, 710049, Shaanxi, China

ARTICLE INFO

Article history:
Received 4 July 2025
Received in revised form
11 January 2026
Accepted 10 February 2026
Available online 13 February 2026

Edited by Min Li

Keywords:
Underground gas storage
Lithologic gas reservoir
Microstructure
Micro-CT
Zonal discrepancy

ABSTRACT

The construction of underground gas storage (UGS) in a large-scale low-permeability lithologic gas reservoir presents an immense engineering challenge. Under the context of UGS, research on structural characteristics and storage capacity at the microscopic scale is insufficient, making it difficult to provide effective support for the engineering scheme. In this study, the microscopic storage spaces of a typical lithologic gas reservoir (i.e., YL block in the Ordos Basin) are comprehensively analyzed through experimental techniques (represented by computed tomography scanning), digital core analysis, and fractal analysis. Furthermore, the feasibility of UGS construction is examined. The results demonstrate that the large-scale low-permeability lithologic gas reservoir exhibits significant zonal heterogeneity in its microscopic structural characteristics at both morphological and statistical levels. Specifically, the microscopic storage spaces of the core zone within the YL block are notably higher than those in the transition and periphery zones, characterized by larger aperture, less tortuous, higher aggregation and connectivity. Consequently, the core zone provides adequate storage capacity and injection-extraction capability for large-scale underground storage of natural gas. In contrast, the transition and periphery zones exhibit inferior microstructural, storage, and flow properties, which are not suitable for rapid injection and production. However, these zones show a fairly strong lateral sealing capability, which can be utilized as a monitoring area to evaluate UGS integrity. These findings indicate that the reservoir's microstructural features meet the essential requirements of storage capacity, injection-extraction capability, and lateral sealing property for UGS construction. Based on this understanding, a series of zone-differentiated UGS engineering suggestions are proposed, including zonal function specification, well type selection, well deployment scheme, and management of old wells. These findings can provide valuable insights for the assessment and implementation of UGS projects from such gas reservoirs.

1. Introduction

Natural gas, as a kind of low-carbon energy, plays a significant role in promoting social progress, optimizing energy structure, and facilitating the green transformation of energy (Bugaje et al., 2022; Dong et al., 2021; Ji et al., 2024; Muhire et al., 2024; Zou et al., 2022, 2024a). In recent years, global natural gas consumption has been increasing year by year (Adebayo et al., 2023; Fan et al., 2022; Zou et al., 2024b). Additionally, the supply-demand relationship for natural gas exhibits obvious seasonal fluctuations (Matar and Shabaneh, 2020; Zhang et al., 2020). Typically, the phenomenon where supply exceeds demand in summer and demand surpasses supply in winter is quite common. The traditional peak regulation mode, reliant solely on gas field production, is difficult to meet the fluctuating peak demand of the natural gas market. Therefore, underground gas storage (UGS), as an

* Corresponding author.
** Corresponding author.
E-mail addresses: tzhua_cq@petrochina.com.cn (Z.-H. Tian), caijc@cup.edu.cn (J.-C. Cai).
Peer review under the responsibility of China University of Petroleum (Beijing).

https://doi.org/10.1016/j.petsci.2026.02.013

important energy storage facility (Liu et al., 2025; Matos et al., 2019; Xiao et al., 2024), operates through a mode of injecting gas during summer and extracting it during winter (Teatini et al., 2011), which demonstrates unique advantages in balancing the supply and demand of natural gas, seasonal peak regulation, and supporting emergency supply when needed.

Since 1915, the construction of global UGS facilities has gone through three stages: initial development, rapid growth, and stable development. According to the statistics from CEDIGAZ (2024), by the end of 2023, there are 681 operational UGS facilities worldwide, forming the working gas volume of 4370×10^8 m^3. The working gas volume accounts for approximately 11%–12% of the global annual natural gas consumption. For some developed countries in Europe and America, this ratio is usually greater than 15% and even exceeds 30%. The exploration of UGS construction in China begins in the 1990s. By the end of 2023, a total of 30 UGSs are built in China, such as DZT, HTB, and XGS, etc (Ban et al., 2023; Liu et al., 2023; Wanyan et al., 2025). These UGSs form the working gas volume of 230×10^8 m^3, accounting for approximately 6% of the annual natural gas consumption in China, which still has a considerable gap compared to the world average level. Considering its gradually increasing demand for natural gas, therefore, continuous evaluation and construction of UGS is still necessary to ensure the stable supply of energy in China (Xie et al., 2023b).

In terms of types of UGSs worldwide, the majority are depleted gas reservoirs (accounting for approximately 67% in number and 75% in working gas), followed by salt caverns and aquifers (Al-Shafi et al., 2023; Soroush and Alizadeh, 2008; Yang et al., 2023). The conversion of depleted gas reservoirs into UGSs possesses the following significant advantages: (1) Clear geological features and abundant production data. (2) The sealing property of the structural trap is often reliably established (Ma et al., 2018; Zhang et al., 2026a; Zhao et al., 2024). (3) Production wells that meet the necessary criteria can be continuously utilized (Bai et al., 2018). Consequently, the gas reservoirs at the end of the development stage are the primary site selection targets for underground energy storage projects, not only for natural gas, but also for hydrogen, compressed air, and other fluids (He et al., 2024; Kushnir et al., 2012; Sekar et al., 2023; Yang et al., 2024; Zhang et al., 2026b). However, as a significant proportion of high-quality depleted gas reservoirs (porosity and permeability over 15% and 50 mD, respectively) have been converted into UGSs, the geological and petrophysical conditions of the remaining available sites of UGS are becoming increasingly poor (Singh, 2022; Tian et al., 2025). Among them, low-permeability lithologic gas reservoirs are an important type of construction target. Compared with the structural gas reservoirs, low-permeability lithologic gas reservoirs are usually characterized by large-scale, low-porosity, low-permeability, and strong heterogeneity (Wanyan et al., 2025).

The construction of UGS from large-scale low-permeability lithologic gas reservoir faces two primary scientific challenges (Li et al., 2023; Xia et al., 2023): (1) Sealing property of the geologic body. There are no structural boundaries for lithologic gas reservoirs. Hence, there is uncertainty regarding whether the lithological boundaries can provide effective lateral sealing capabilities, which in turn affects the safe and efficient operation of UGS. (2) Productivity of gas wells or operation efficiency of UGS. Strong heterogeneity (Qiao et al., 2021) and poor petrophysical properties result in generally low well productivity, but some wells have relatively good production capacity. The traditional overall construction mode for UGS based on structural reservoirs will lead to low operational efficiency. The above key issues directly determine the feasibility of UGS construction from large-scale low-permeability lithologic gas reservoirs. The fundamental issue lies in understanding the microstructural properties of these reservoirs, which determine their lateral sealing property, petrophysical property, and well productivity (Bahrami et al., 2024; Lyu et al., 2025; Qiao et al., 2020; Saeed and Jadhawar, 2024). Therefore, it is necessary to conduct a comprehensive study on low-permeability lithologic gas reservoirs from a microscopic perspective to demonstrate their feasibility for UGS construction.

This study takes the YL block in the Ordos Basin of China as a representative example. Its microscopic storage spaces are characterized by the combination of experimental tests, digital core analysis, and fractal geometry analysis. The general characteristics, zonal discrepancies, and controlling factors of microscopic storage spaces are revealed. From the perspective of microscopic level, the feasibility of converting large-scale low-permeability lithologic gas reservoirs into UGSs is demonstrated. In addition, several zone-differentiated engineering suggestions are proposed for UGS construction.

2. UGS construction and geological background

The Ordos Basin is the second largest petroliferous basin in China. The widely distributed low-permeability lithologic gas reservoirs make it an ideal place for theoretical research and practical application of UGS construction (Zhang et al., 2023; Zou et al., 2012). There are two main gas-producing strata, namely, the Lower Paleozoic carbonate rocks (represented by the Majiagou Formation) and the Upper Paleozoic clastic rocks (represented by the Shanxi Formation) (Du et al., 2019; Li et al., 2019; Xie et al., 2023a), which are also the target layers for UGS construction. The construction of UGS in this basin has the following notable advantages: (1) Located in China's largest natural gas production base (He et al., 2022), the gas supply is guaranteed. (2) Situated at the central hub of the onshore natural gas pipeline network (Wen et al., 2022), the long-distance pipeline network is well-equipped, ensuring the safe transmission of natural gas. (3) The geological feature is relatively simple, with few or without faults, weak or without edge-bottom water, making the UGS construction relatively easier.

To explore feasible technical solutions for converting large-scale low-permeability lithologic gas reservoirs into UGSs, in 2022, a novel “three zones” collaborative construction mode of UGS is presented and is first applied to the construction planning of YL UGS, Ordos Basin (Wang et al., 2022). Under the index evaluation system of “five-facies” (namely, sedimentary facies, diagenetic facies, petrophysical facies, seepage structure facies, and flow unit facies) (Wang et al., 2022), the construction area of YL UGS is divided into the core zone, transition zone, and periphery zone (Fig. 1). The specific evaluation indicators and criteria of the “three zone” division are elaborated in detail in the literature of Wang et al. (2022). Therefore, this article does not repeat them here. Among them, the core zone mainly functions for gas injection and production; the transition zone considers both collaborative gas extraction and dynamic monitoring, while the periphery zone mainly serves the purpose of dynamic monitoring.

Next, we briefly introduce the geological features of the study area. As displayed in Fig. 1(a) and (b), the YL block is situated in the northeast part of the Ordos Basin, near Yulin City, covering an area of over 120 km^2, which is a typical large-scale low-permeability sandstone lithologic gas reservoir. It is located at the northeast of the Yishaan Slope, where the west-dipping monocline exhibits an angle ranging from 0.15° to 1° (Jiang et al., 2016; Li et al., 2019). During the gas development stage, the Shanxi Formation is the main producing layer, which is a constant-volume sandstone lithologic gas reservoir. In the UGS evaluation stage, the target construction layer of YL UGS is the $Shan_2^3$ sub-member (Fig. 1(c)). The buried depth of the $Shan_2^3$ sub-member in the YL block ranges from 2865.10 to 3245.40 m, averaging 2962.82 m. The effective

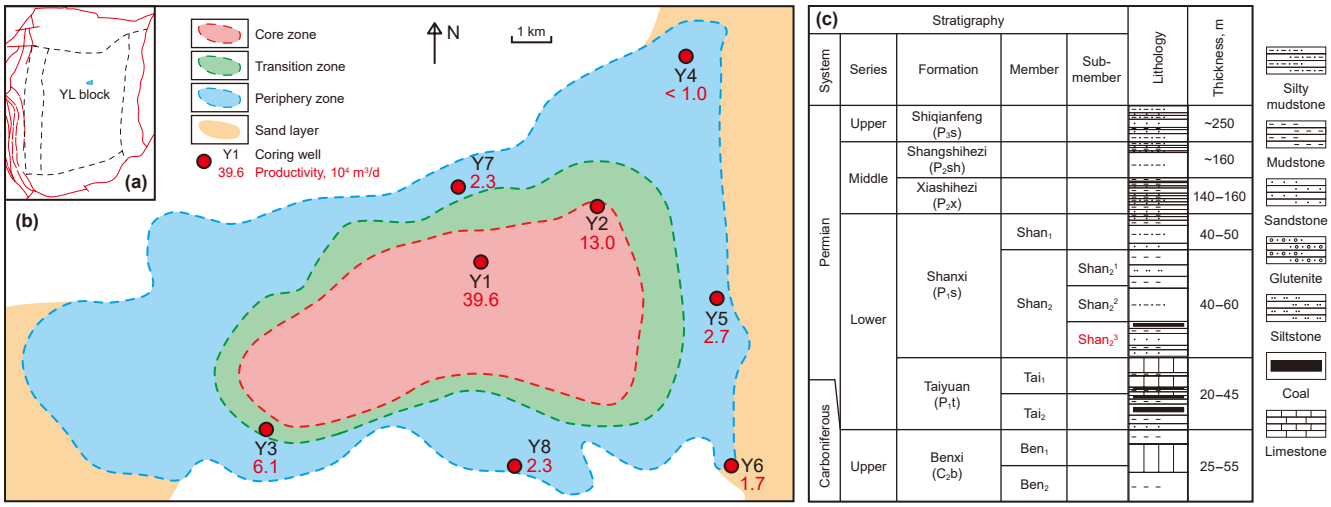

Fig. 1. **(a)** Location of YL block, **(b)** zone division of YL UGS and location of sampling wells, and **(c)** stratigraphic information of Carboniferous to Permian in the Ordos Basin (in which the stratum marked in red is the target layer for UGS construction).

thickness of the $Shan_2^3$ sub-member is between 3.1 and 21.9 m, with an average of 10.1 m. The $Shan_1$ member and $Shan_2^{1-2}$ sub-member are the direct caprock for the gas reservoir, while the Taiyuan Formation serves as the base layer of the gas reservoir.

3. Samples and methods

3.1. Samples

A total of 22 sandstone samples from 8 wells in the YL UGS area are collected. As shown in Fig. 1, the distribution of coring wells is relatively even. All the collected samples originate from the $Shan_2^3$ sub-member, with their burial depths ranging between 2881.7 and 3030.9 m. These samples span the core zone, transition zone, and periphery zone of YL UGS.

3.2. Experimental analyses

At present, a relatively comprehensive set of experimental methods for characterizing reservoir properties and microstructure has been established. The classification, theory, and application of these methods are elaborated in the review literature (Anovitz and Cole, 2015; Arif et al., 2021; Blunt et al., 2025; Cnudde and Boone, 2013; Guo et al., 2020; Lai et al., 2018), and will not be repeated here. To analyze the petrophysical and microstructural properties in different zones of YL UGS, the following experimental tests are carried out on these sandstones, including porosity test, permeability test, nuclear magnetic resonance (NMR) analysis, X-ray diffraction (XRD) analysis, scanning electron microscopy (SEM) imaging, and computed tomography (CT) scanning (Fig. 2). The main experimental setups and processing procedures are as follows:

(1) The porosity of cylindrical samples (2.5 cm in diameter and 5.0 cm in length) is tested by the gravimetric method. The saturated fluid is ethyl alcohol with a density of 789 kg/m^3 at the test temperature of 20 °C. By the ratio of the quality difference between the saturated and dried sample to the sample volume, the porosity of the samples can be obtained.
(2) The permeability of cylindrical samples is analyzed by the steady-state method. The experimental temperature is 20 °C, the outlet pressure is set at 0.10 MPa, and the inlet pressure is between 0.30 and 1.06 MPa, depending on the petrophysical property and experimental condition. To reduce the test error, at least three rounds of permeability tests are conducted. When the ratio of the standard deviation to the average value is less than 0.05, the result of permeability takes the average value. Otherwise, the test result that deviates the most from the average value should be excluded until the ratio of the standard deviation to the average value meets the above requirement.
(3) The NMR analysis is conducted on three typical water-saturated cylindrical samples from wells Y1, Y3, and Y8. The measurement is conducted using a Spinsolve 60 Ultra instrument with a working frequency of 60 MHz. The experiment temperature is maintained at 30 °C, the echo interval, waiting time, and scan times are 0.1 ms, 5000 ms, and 64, respectively.
(4) The two-dimensional (2D) microstructure of typical sandstones from wells Y1 and Y8 is imaged by SEM, the magnifications are between 500 and 1500 times, and the imaging mode is secondary electron imaging.
(5) The three-dimensional (3D) microstructure of sandstones is obtained by an Xradia 610 Versa-type CT scanner, providing a limiting resolution of 300 nm. In this study, 5 representative samples (i.e., Y1-C, Y2-C, Y3-C, Y6-C, and Y8-C) from different zones of YL UGS are scanned at a resolution of 1.5 μm per voxel. The size of these raw micro-CT images is 988 pixels × 1013 pixels × 797 pixels, corresponding to the physical size of 1482 μm × 1519.5 μm × 1195.5 μm. The image processing and analysis are performed by Avizo® 3D software, including denoising, cropping, binarization, pore network model (PNM) generation, image display, and data statistics, etc. Among them, the median filter method is used to reduce the noise in the image. For the image binarization process, the interactive thresholding method is adopted to distinguish the pores from the matrix. The connected pores in the *z*-direction are detected with the "neighborhood" option of 6, which means voxels with a common face are considered connected. For the PNM generation process, the Chamfer-Conservative method, maker extent of 0, and repeatable algorithm mode are adopted, the interpretation

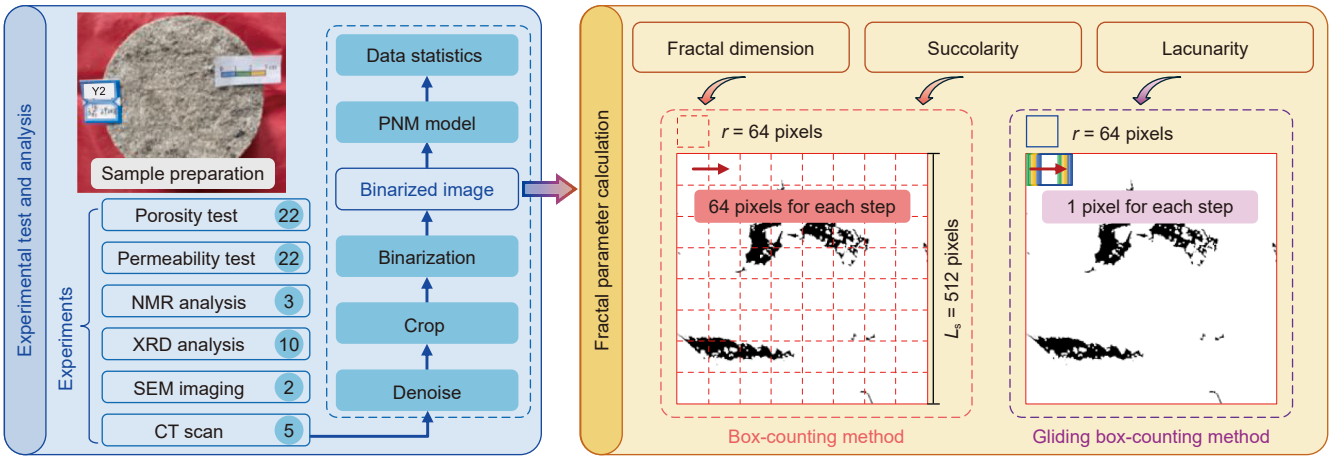

Fig. 2. Flowchart of experimental analysis and schematic diagram of calculation methods for fractal parameters. The number of tested samples is indicated next to the experimental tests.

and neighborhood options use default values, to generate the connected objects. In this study, cubic digital cores with a side length of 512 pixels (physically 768^3 μm^3) are cropped from the raw cylindric CT images to perform the microstructural properties analysis.

3.3. Fractal parameters calculation

Due to its advantages in non-linear quantization representation, in recent years, the fractal geometry theory has been increasingly adopted in the fields of geoscience and life science (Bushell et al., 2002; Datseris et al., 2023; Nayak et al., 2019; Sendker et al., 2024; Tian et al., 2021; Zang et al., 2022). To further quantitatively characterize the microstructures of sandstones of YL UGS, multiple fractal parameters are adopted in this study, including the fractal dimension (D_f), lacunarity (Λ), and succolarity (Su) (Allain and Cloitre, 1991; Cai et al., 2024; de Melo and Conci, 2013; Ding et al., 2023; Roy et al., 2010; Xia et al., 2019). These parameters are the measures of pore complexity, heterogeneity, and connectivity, respectively. In this study, these fractal parameters are obtained by analyzing the binarized cubic CT images with self-coded programs. The following are the brief definitions of and calculation methods for these fractal parameters:

(1) Fractal dimension is the measure of the complexity of objects, such as pores or matrices of natural rocks. In this study, the pores in sandstones are objects of concern, because they are the gas storage spaces for UGS. For the binarized 2D and 3D images, the fractal dimension of pores is usually measured by the box-counting method (Cai and Hu, 2015; Feder, 1988; Xia et al., 2019) (Fig. 2). The basic principle of this method is to cover the binary 2D (or 3D) images with square (or cubic) boxes. The side length of these boxes is defined as r. When the boxes with different size lengths r cover a 2D or 3D image, denote the number of boxes that contain the pores as $N(r)$. By fitting $N(r)$ with r according to the following formula, the fractal dimension can be obtained, which is the negative slope of the fitting line.

$$\log N(r) = -D_f \log r + C \tag{1}$$

where C is a constant. In this paper, the fractal dimensions of 2D slices ($D_{f\ 2D}$) and 3D images ($D_{f\ 3D}$) are calculated, and the side length of these images (L_s) is 512 pixels.

(2) Lacunarity is a fractal parameter describing the degree of aggregation of research objects. A larger lacunarity means the distribution of research objects is more concentrated, and vice versa. Lacunarity can be calculated by the gliding box-counting method. A brief description of this method is illustrated in Fig. 2. Compared with the box-counting method, the boxes only move 1 pixel for each step for the gliding box-counting method. In addition, a more specific calculation process of the algorithm can be referred to in the literature of Allain and Cloitre (1991) and Xia et al. (2019). Lacunarity is defined as:

$$\Lambda(r) = \frac{Z_Q^{q=2}(r)}{\left[Z_Q^{q=1}(r)\right]^2} \tag{2}$$

where $\Lambda(r)$ is the lacunarity of square or cubic boxes with varying side lengths of r for 2D and 3D images, respectively. Z_Q^q is the statistical moment function with different q. The value of lacunarity can be affected by porosity, to eliminate this effect, the normalized lacunarity ($\Lambda^*(r)$) is calculated herein:

$$\Lambda^*(r) = \phi \frac{\Lambda(r) - 1}{1 - \phi} \tag{3}$$

where ϕ is porosity.

(3) Succolarity can quantitatively characterize the connectivity of research objects in different directions, which can be obtained by the box-counting method. The basic idea of this method is assuming that there is a virtual pressure field along the directions of fluid flow, using square or cubic boxes with varying side lengths r to cover the image, recording the ratio of the permeable area (or volume) to the box area (or volume) ($OP(r)$) and the virtual pressure at the center of the boxes at different positions ($PR(r, pc)$). Then, the succolarity in different directions and for varying r can be calculated through the following formula (de Melo and Conci, 2013):

$$Su_{\mathrm{dir}}(r) = \frac{\sum_{i=1}^{n} OP(r)PR(r, pc)}{\sum_{i=1}^{n} \max OP(r)PR(r, pc)} \tag{4}$$

where dir is directions; and n is the number of boxes whose side length equals r. Detailed calculation processes and examples can be referred to in the literature of de Melo and Conci (2013).

4. Results

4.1. Composition of sandstones

As displayed in Fig. 3(a), the $Shan_2^3$ sandstones in different zones of YL UGS are primarily composed of quartz, coupled with minor amounts of clay minerals and a small proportion of carbonates and siderite. Additionally, discrepancies are observed between the mineral compositions of sandstone in the core and periphery zones of YL UGS (Fig. 3(b)). Specifically, the average quartz content in the core zone is greater than that in the periphery zone. However, the situation is inverse for clays, since the periphery zone exhibits over 1.75 times the clay mineral content compared to the core zone. These variations in mineral composition in different zones are also corroborated by the SEM images presented in Fig. 4. The well Y1 in the core zone is predominantly composed of quartz grains with diameters ranging from several to tens of microns, and almost no clay minerals are detected. While for the typical well Y8 in the periphery zone, appreciable clay minerals are present alongside quartz grains. The diameter of these clays is mostly no more than 3 μm, which is significantly smaller than the size of the quartz grains. In addition to observing minerals, these SEM images show that the sandstone mainly develops intergranular pores.

4.2. Porosity and permeability of cylinder cores

The porosity and permeability of the target construction layer for UGS are important petrophysical properties for the storage capacity and injection-production performance assessment. As shown in Table 1, the experimental results for the sandstones from YL UGS exhibit significant variations in both porosity (0.89% to 8.33%) and permeability (0.03 to 2.10 mD), presenting the characteristics of low-porosity and low-permeability. These findings present substantial challenges for the construction and operation of YL UGS, as they are essentially the result of intricate interactions involving parameters such as porosity and permeability. Given this complexity, it becomes imperative to conduct in-depth analysis of these petrophysical properties, not only to gain deeper insights into their essential characteristics but also to provide effective strategies for the successful construction and efficient operation of UGS.

Through the intersection relationship analysis between porosity and permeability, it is found that there is a positive porosity-permeability correlation for the sandstones with permeability greater than 0.1 mD (Fig. 5). Moreover, most of the sandstones in the core zone possess superior gas storage capacity (porosity >3.6%) and higher flow capacity (permeability >1 mD) compared to those in the transition and periphery zones. Based on this, it is inferred that the microscopic pores in the core zone may have relatively higher connectivity. In contrast, the transition and periphery zones show a lower porosity range (mostly below 4.0%), yet their permeability spans two orders of magnitude (0.01 to 1 mD). This indicates that the pore connectivity is more complex in these zones. For instance, sample T1 from the periphery zone demonstrates minimal porosity in the total 22 sandstones, but displays a flow capacity comparable to core zone samples, suggesting relatively good pore connectivity despite its poor porosity. On the contrary, sample T2 possesses the largest porosity within the periphery zone samples, but its flow capacity is almost the lowest, implying a weak pore connectivity. The above analysis of pore connectivity in different zones is a preliminary and qualitative inference based on the porosity-permeability correlation. In the following sections, the quantitative assessment of pore connectivity in different zones of YL UGS is further performed by digital core and fractal parameter analysis.

The statistical data of porosity and permeability will reflect the general characteristics of the samples. For porosity, the average, median, and maximum values decrease from the core zone to the transition zone and periphery zone (Fig. 6). This indicates a progressive decline in gas storage capacity with increasing distance from the core zone. The permeability is significantly higher in the core zone compared to the transition and periphery zones, suggesting a better flow capability. Moreover, both transition and periphery zones show similar flow capacity. The rather high standard error for the average values of porosity and permeability indicates the distribution of petrophysical properties is relatively scattered, which may be due to limited sample quantity and the heterogeneity of the reservoir. Even so, based on the variation trend of these statistical parameters, it is concluded that the core zone serves as the primary gas storage and production area, while the gas storage and injection-production capacity is relatively weak for the transition and periphery zones. However, the transition and periphery zones should not be viewed as completely disadvantageous for the construction of lithologic gas reservoir-

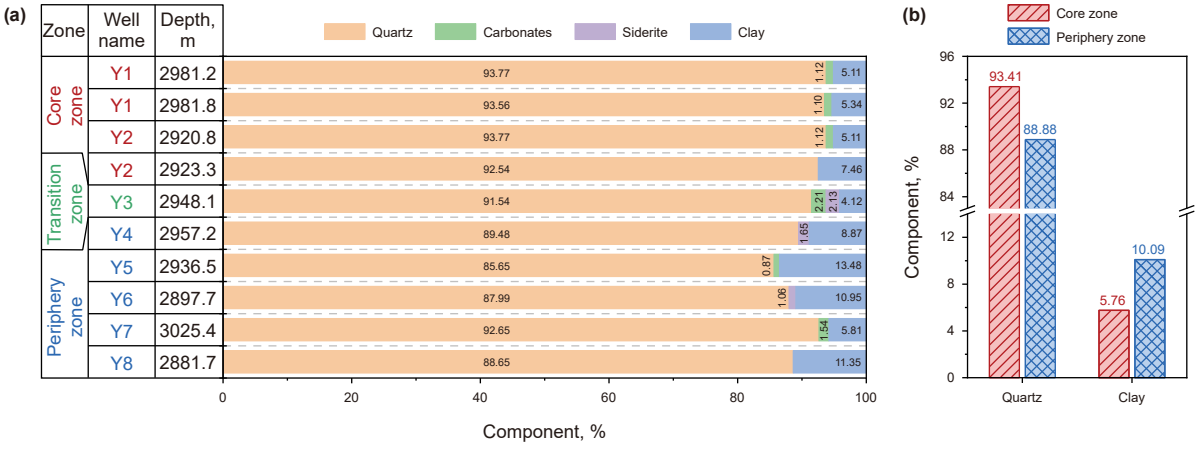

Fig. 3. Composition of sandstones in different zones of YL UGS. **(a)** XRD analysis results, **(b)** average contents of quartz and clay in the core and periphery zones.

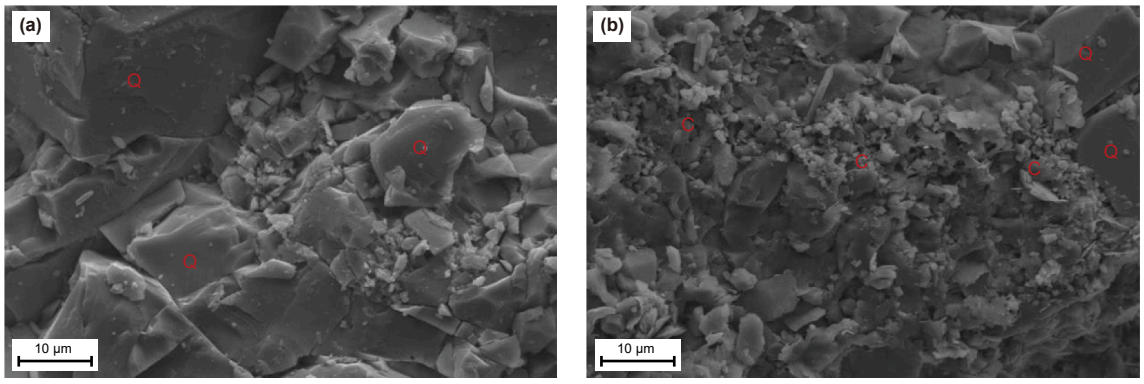

Fig. 4. SEM images of typical sandstones of YL UGS. Q: quartz, C: clay. **(a)** Well Y1, 2981.2 m, and **(b)** well Y8, 2881.7 m.

Table 1
Porosity and permeability of sandstones in different zones of YL UGS. The relative error of the porosity measurement is less than 1%.

Zone	Well name	Depth, m	Porosity, %	Permeability, mD	Standard error of permeability
Core zone	Y1	2981.2	8.33	2.10	0.0035
	Y1	2981.8	7.70	1.36	0.0012
	Y2	2918.6	4.27	0.75	0.0054
	Y2	2920.8	3.86	1.10	0.0262
	Y2	2923.3	4.19	2.09	0.0342
	Y2	2925.0	4.21	1.15	0.0026
	Y2	2926.7	0.90	0.68	0.0043
Transition zone	Y3	2947.2	4.49	1.36	0.0196
	Y3	2947.9	1.22	0.09	0.0008
	Y3	2948.1	4.10	0.04	0.0009
	Y3	2949.1	2.55	0.04	0.0007
Periphery zone	Y4	2957.2	2.34	0.66	0.0161
	Y4	2958.0	3.28	0.06	0.0007
	Y5	2936.5	0.89	0.71	0.0187
	Y5	2938.6	1.52	0.21	0.0050
	Y6	2899.5	3.29	0.07	0.0001
	Y6	2897.7	4.17	0.03	0.0002
	Y7	3025.4	3.52	1.43	0.0697
	Y7	3028.4	3.52	0.92	0.0034
	Y7	3030.9	2.37	0.17	0.0019
	Y8	2882.4	3.00	0.05	0.0002
	Y8	2881.7	2.35	0.03	0.0004

type UGS. It mainly includes the following two aspects of consideration: (1) the gas storage volume in the transition and periphery zones is relatively small, which can reduce the demand for cushion gas, and (2) the lower permeability can provide the lateral sealing function between the core zone and the external geological bodies, reducing gas leakage risks. For the geological engineering design of a UGS, the transition and periphery zones can play a role in lateral sealing or blocking for natural gas.

4.3. Microscopic structure of gas storage spaces

4.3.1. Qualitative insights from digital cores

In this section, the microstructural characteristics of sandstones in different zones of YL UGS are analyzed utilizing micro-CT and digital core technology. The 3D microstructure of 3 representative sandstones is illustrated in Fig. 7. By observing these images, the preliminary qualitative cognition on the sandstone microstructures in different zones of YL UGS is obtained. As shown in Fig. 7(b), the pore volume decreases from samples Y1-C to Y3-C and Y8-C, indicating a declining trend of gas storage capacity from the core to transition and periphery zones. Additionally, the core zone develops larger pores with higher degrees of aggregation compared to the transition and periphery zones. Essentially, pores that are interconnected play a significant role in gas storage and production, while the isolated pores are essentially inert during the production stage of a reservoir and the operation stage of a

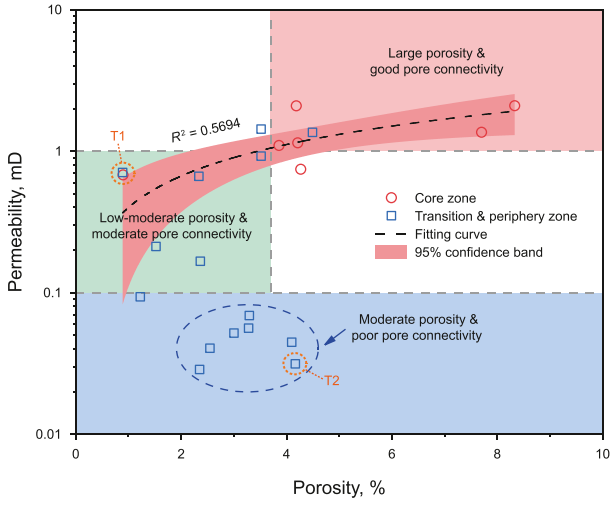

Fig. 5. Porosity versus permeability of sandstones in YL UGS.

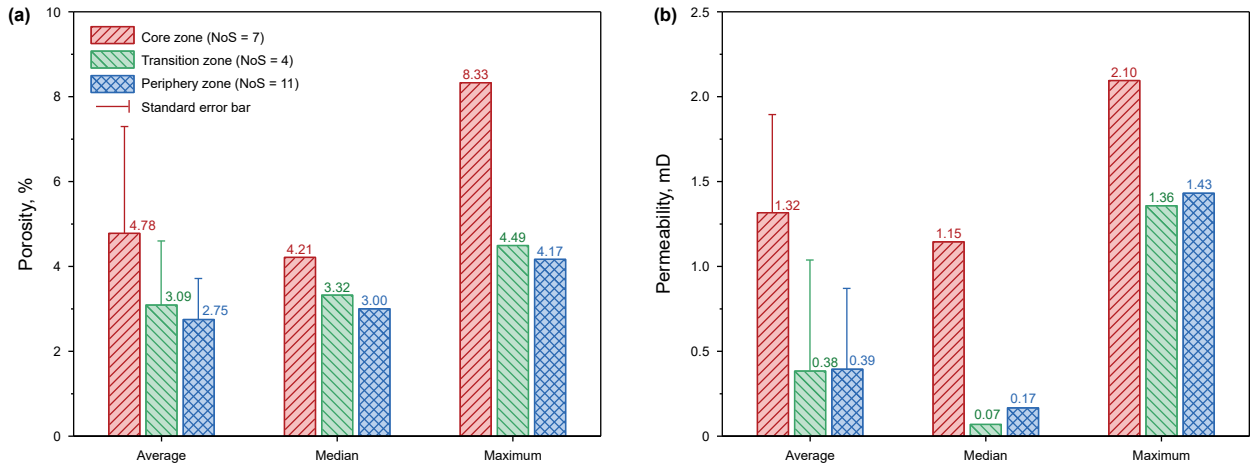

Fig. 6. Statistical parameters of **(a)** porosity and **(b)** permeability of sandstones in different zones of YL UGS. Nos denotes the number of samples.

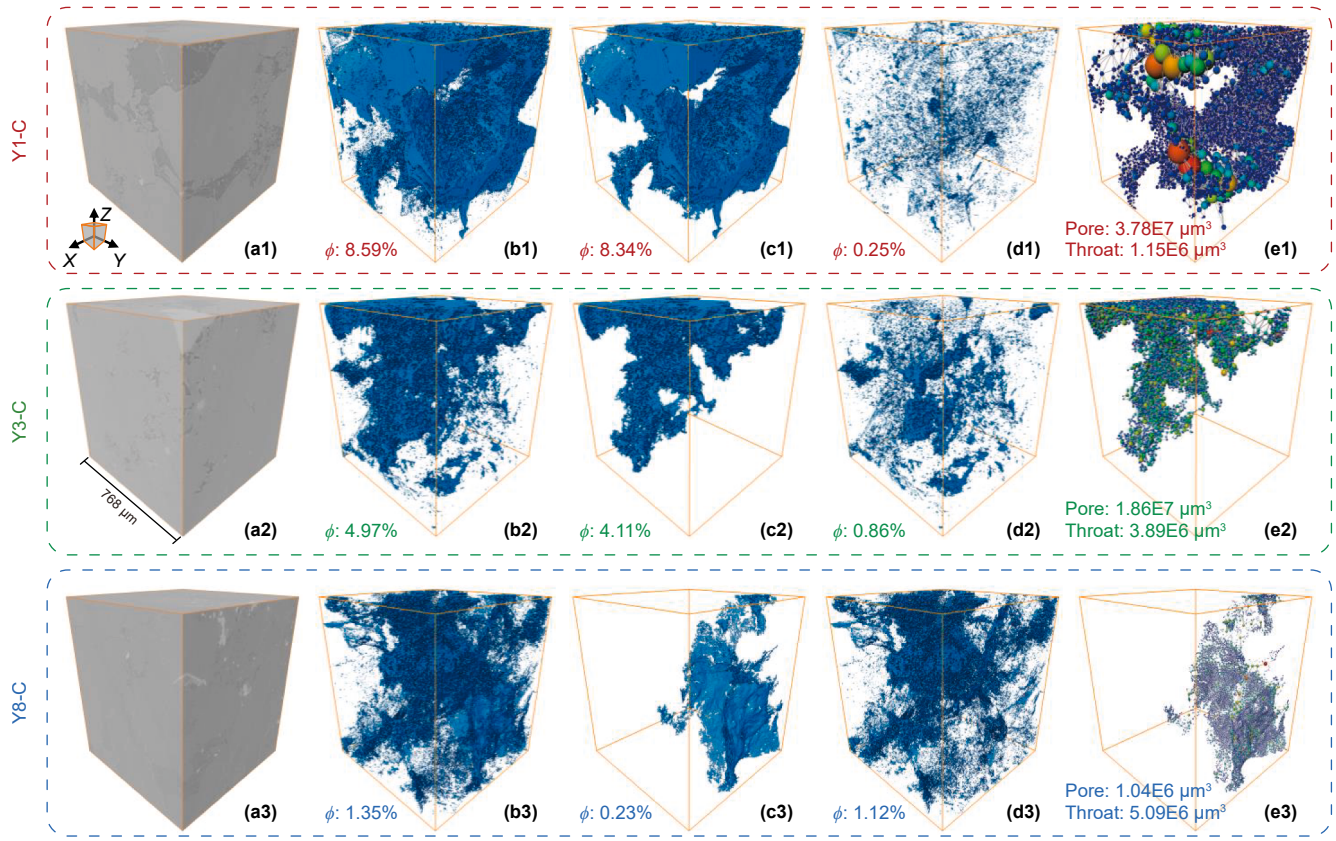

Fig. 7. **(a)** Cropped raw grayscale micro-CT images, **(b)** pores in the digital cores, **(c)** connected pores in the digital core (*z*-direction), **(d)** isolated pores in the digital core, and **(e)** PNM models, where the pores are displayed as different-colored and different-sized balls according to equivalent pore radius, while the throats are displayed in the same width and color. The physical size of the digital cores is 768 × 768 × 768 μm^3. The ϕ values in (b) to (d) are total porosity, porosity of connected pores, and porosity of isolated pores, respectively. The numbers in (e) are the pore volume and throat volume of PNM models.

UGS. To further analyze these behaviors, connected pores are extracted from the digital cores (Fig. 7(c)). It is revealed that the volume and connectivity of pores in the core zone are superior, and clumpy and clustered distributed. In contrast, the transition and periphery zones exhibit fewer connected pores, which are banded and lamellar distributed. In addition, the pores and throats are extracted by the PNM model (Fig. 7(e)). For the PNM model of core zone sample Y1-C, a set of large-sized pores is extracted, and the pore size distribution displays stronger heterogeneity due to a wider range of equivalent pore radius compared with Y3-C and Y8-C samples. Conversely, the pores are smaller and more evenly distributed for the sandstones in the transition and periphery zones, showing a weaker heterogeneity in pore size distribution. As shown in Fig. 7(d), from core to transition and periphery zone, the volume of isolated pores significantly increases, and these pores are dotted to clustered distributed. The above findings reveal the general characteristics and their differences for the pore spaces in different zones of YL UGS from a qualitative perspective.

4.3.2. Pore spaces and their classifications

To further elucidate the storage capacity of different zones within YL UGS, the porosity and its classifications of three representative sandstones are evaluated. As shown in Fig. 8(a), from the core zone to the periphery zone, the porosity gradually decreases, which is consistent with the statistical pattern in Fig. 6(a). It should be noted that the pore with a size smaller than 1.5 μm cannot be characterized in the digital core because of the resolution limit of the micro-CT scan. If their high-precision full-scale pore size distribution curves are obtained, such as with the help of nano-CT, focused ion beam SEM, or mercury intrusion porosimetry (Garum et al., 2020; Saif et al., 2017; Zheng et al., 2022), the proportion of missing pores can be quantified. Since the full-scale pore distribution curves are inaccessible in this paper, the missing pores cannot be evaluated quantitatively. In addition, there are certain differences in the porosity obtained by the three methods. Existing studies have conducted in-depth analysis on this phenomenon (Yuan and Rezaee, 2019; Zhao et al., 2022; Zhou et al., 2021). It is mainly due to the different detection objects, different detection resolutions, and different sample scales of these three porosity analysis methods. Even so, the relative values of porosity obtained by the different methods for these three samples are similar, which reflects the differences in pore spaces within different zones to some extent (Fig. 8(a)).

From the perspective of pore size, qualitatively, the pore size in the sandstones shows a bimodal distribution pattern, indicating the presence of two different-sized pores (Fig. 8(b)). Interestingly, from the core zone to periphery zone, the transverse relaxation time (T_2) corresponding to the main peak and secondary peak both decrease. Their average pore size also gradually decreases if they have the same T_2-pore size conversion relationship. However, there is still controversy over whether NMR data can accurately quantify the characteristics of pore size distribution, due to the uncertainty and subjectivity of parameters such as surface relaxation rate and shape factor, as well as the complexity of T_2-pore radius conversion relationships (Jiang et al., 2023). Therefore, the pore size distribution curves are not calculated from NMR data in this paper.

From the perspective of pore connectivity, the pores in the digital core can be categorized into connected pores and isolated pores. As shown in Fig. 8(c), the porosity of connected pores is 8.34%, 4.11%, and 0.23%, respectively, which corresponds to a similar decrease trend observed in Fig. 7(b). On the other hand, the proportion of isolated pores in these digital cores is increasing from 2.95% in the core zone, to 17.28% in the transition zone, and to 83.02% in the periphery zone. The increase in isolated pores will assuredly influence the gas storage capacity.

According to the porosity and its classification, it is concluded that the sandstone in the core zone possesses higher gas storage capacity, average pore size, and potential utilization degree of pore space, while the transition and periphery zones show diminished gas storage capacity.

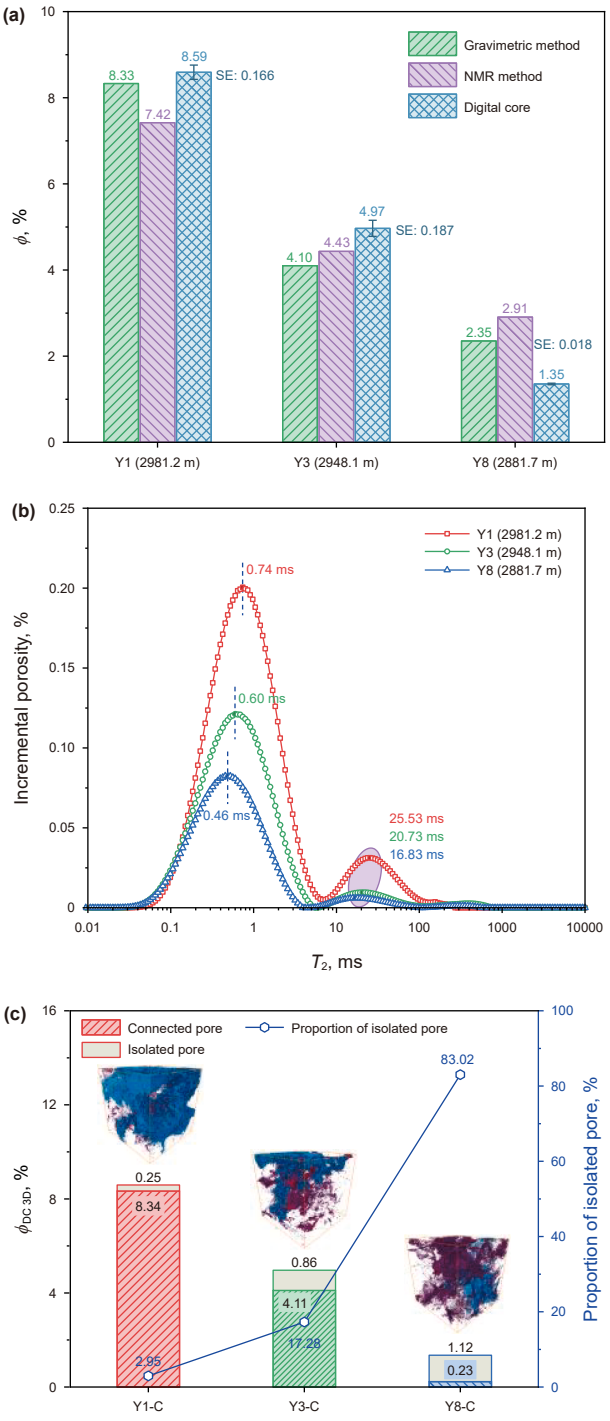

Fig. 8. **(a)** Porosity analyzed by different methods; **(b)** Incremental porosity analyzed by NMR measurement; **(c)** Pore space classifications of digital cores in different zones of YL UGS. SE represents the standard error, and $\phi_{DC\ 3D}$ is the porosity of the digital core.

4.3.3. Insights from PNM model

The PNM model is a commonly used tool in porous media characterization, which can provide quantitative analysis of the distribution of pores and throats for the connected components at the pore-scale. Herein, the distribution histograms of pores and throats for the sandstones in different zones are obtained based on PNM models (Fig. 9). The pore volume is unimodally distributed for core and transition zone sandstones in the log-log plot, as shown in Fig. 9(a), with most of the pores distributed in the range of 10^2 to 10^4 μm^3. While the periphery zone develops a mass of small-sized pores whose volumes are less than 100 μm^3. In addition, the equivalent pore radius, equivalent throat radius, and throat length of these PNM models are overall unimodally distributed with positive skewness (Fig. 9(b)–(d)), indicating that small-sized pores and throats are abundant in different zones of YL UGS. The pore size distribution pattern shown in Fig. 9(b)–(d) is different from that in Fig. 8(b), which is due to the following aspects (Jiang et al., 2023; Zhao et al., 2022): different characterized objects (pore and throat from PNM model vs. pore that filled with H^1 containing fluids), different detection range (micron-sized pore

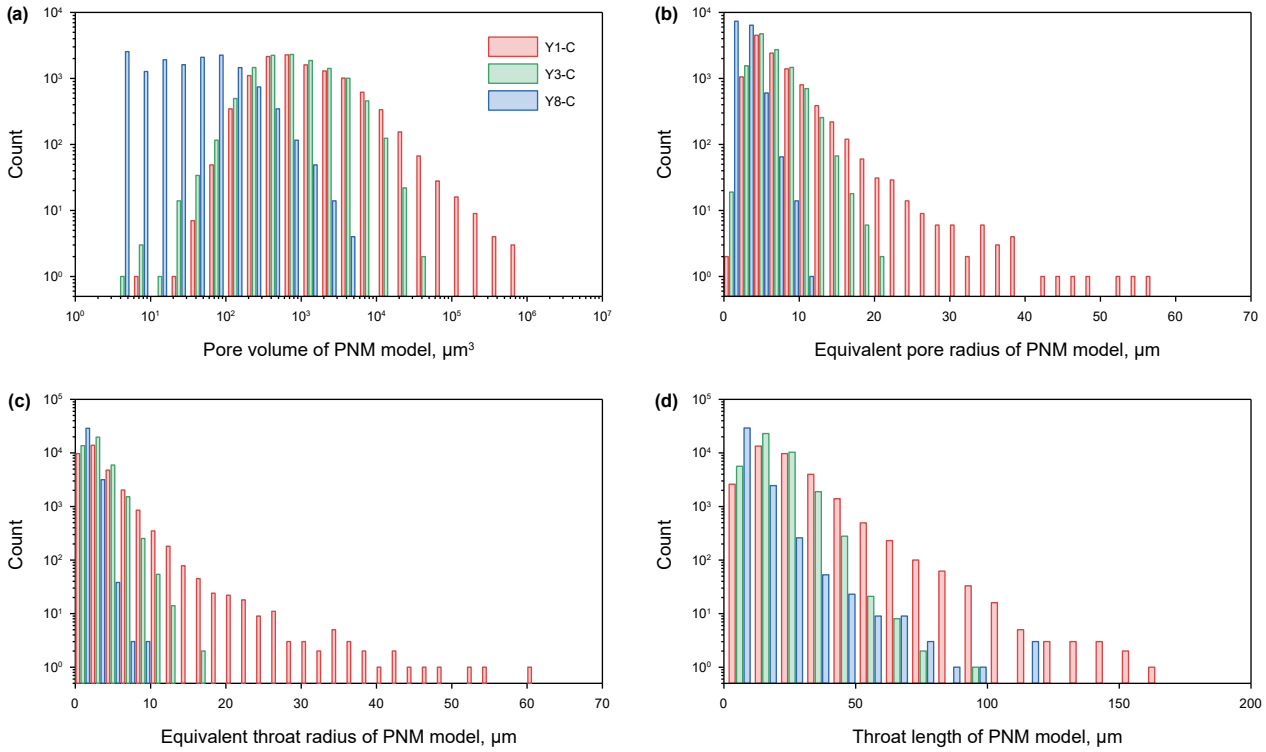

Fig. 9. Pore size distribution for sandstones in different zones of YL UGS. **(a)** Pore volume distribution, **(b)** pore radius distribution, **(c)** throat radius distribution, and **(d)** throat length distribution.

vs. full-sized pore), different measure (count of pore and throat vs. incremental porosity), and different sampling intervals. Even so, the core zone shows the widest distribution range and largest values for all the parameters shown in Fig. 9, indicating a better petrophysical property. This understanding is the same as the result shown in Fig. 8(b).

Statistical parameters presented in Fig. 10 corroborate the zonal discrepancies in microstructures of sandstones within YL UGS. The analysis demonstrates that the microstructural properties of Y3-C are slightly inferior compared to Y1-C, while pronounced differences in these statistical parameters can be observed between Y1-C and Y8-C. Therefore, it is demonstrated that from core zone to periphery zone, the size of the storage spaces gets smaller, and the pore shapes get narrower and more tortuous, indicating a reduction in gas storage and flow property and an enhancement in fluid flow resistance.

From the analysis of the digital cores, the sandstone in the core zone within YL UGS is characterized by superior gas storage spaces, a higher proportion of connected pores, wider distribution and larger average values for pore and throat, and lower length-width ratio and tortuosity for pores, which can store large amounts of natural gas and demonstrate rapid gas injection-production potential required by the UGS.

4.4. Fractal characteristics of gas storage spaces

4.4.1. Fractal dimension and complexity of pores

The fractal dimensions of 2D slices ($D_{f\,2D}$) and their distribution ranges are displayed in Fig. 11 and Table 2. The $D_{f\,2D}$ values are all distributed in the range of 0 to 2, which is consistent with the fundamental principles of fractal geometry theory (Mandelbrot, 1982; Tian et al., 2021; Yu and Cheng, 2002). The larger the fractal dimension, the more complex the pore distribution becomes. Specifically, the core zone sample exhibits larger fractal dimensions, indicating greater spatial complexity in the pore structure. This type of complexity is usually associated with the quantity of pore volume. In addition, the analysis of variance (ANOVA) is performed using the Excel software to investigate the significance of the fractal dimension. The significance level (α) of 0.05 is selected to calculate the P value among core, transition, and periphery zones. It is found that P values are less than 2.98×10^{-9}, indicating a significant change in fractal dimension among different zones.

As illustrated in Fig. 11(b), there is a positive correlation between $D_{f\,2D}$ and the porosity of 2D slices ($\phi_{DC\,2D}$). Essentially, if the pore size distribution of porous media satisfies the statistical self-similarity characteristics, the following scaling law is then satisfied (Yu and Li, 2001).

$$D_f = d_E - \frac{\ln \phi}{\ln\left(\frac{R_{min}}{R_{max}}\right)} \tag{5}$$

where d_E is Euclidean dimension (2 and 3 in 2D and 3D spaces, respectively); R_{min} and R_{max} are the minimum and maximum pore diameters of self-similar intervals, respectively. For convenience, the ratio of R_{min} to R_{max} is further defined as R_r.

Fitting $D_{f\,2D}$ versus $\phi_{DC\,2D}$ with Eq. (5), the prediction of R_r by equation ($R_{r\,EQ}$) with the information of 2D slices is demonstrated to be between 4.12×10^{-3} and 6.16×10^{-3}, as shown in Table 2. The values of $R_{r\,EQ}$ are less than 0.01, further, $(R_{min}/R_{max})^{D_f} \approx 0$ also holds, which means that these sandstones are suitable for the analysis using the fractal geometry theory. In addition, the prediction values of R_r by digital core analysis ($R_{r\,DC}$) with the information in three dimensions also claim to be the magnitude of 10^{-3}, except for sample Y8-C. For most of these sandstones, the prediction values of $R_{r\,EQ}$ and $R_{r\,DC}$ are similar. It is noted that $R_{r\,EQ}$ and $R_{r\,DC}$ are derived based on 2D and 3D information, respectively.

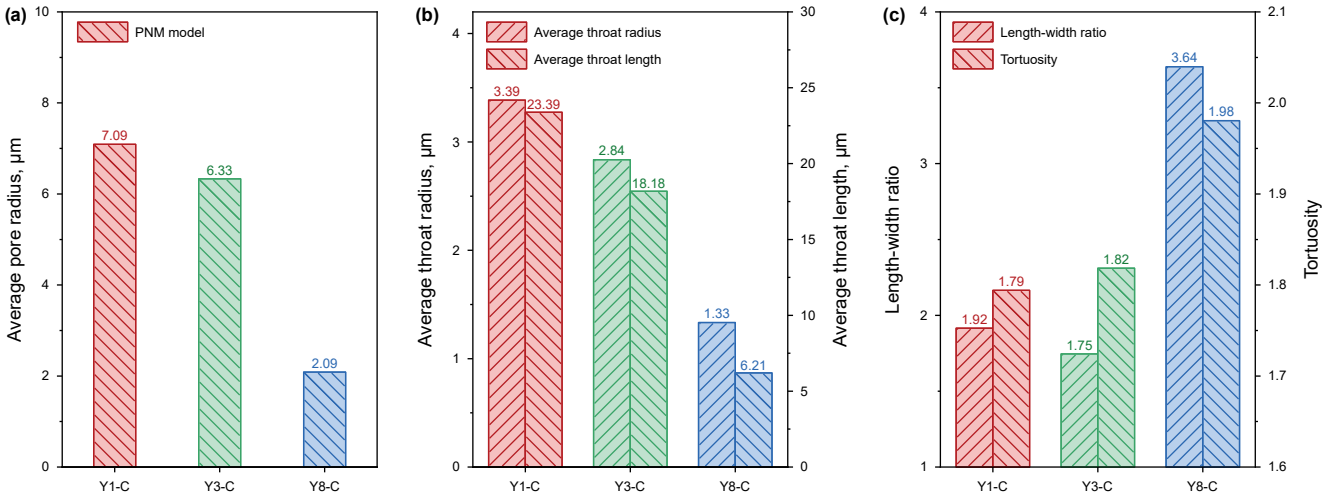

Fig. 10. Statistical parameters of storage space for sandstones in different zones of YL UGS. **(a)** average pore radius of PNM models, **(b)** average values of throat radius and length of PNM models, and **(c)** average values of length-width ratio and tortuosity.

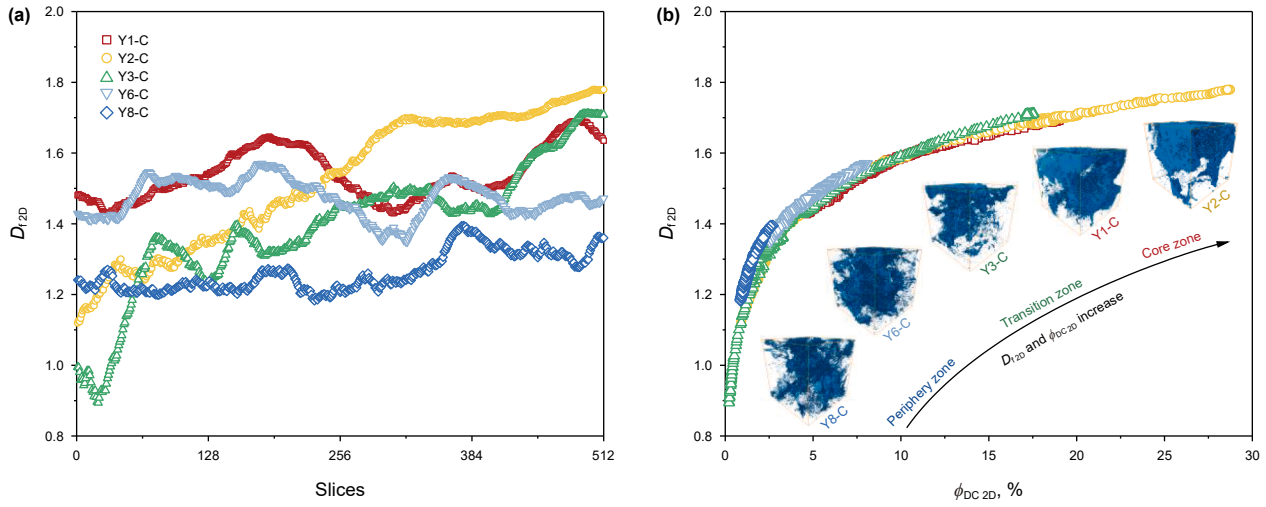

Fig. 11. **(a)** Fractal dimensions of two-dimensional slices and **(b)** plot of porosity versus fractal dimensions for the sandstones in different zones of YL UGS.

Table 2
Distribution range of fractal dimensions and prediction of self-similar intervals.

Sample	$D_{f\,2D}$	$R_{r\,EQ}$	$R_{r\,DC}$	$R_{r\,EQ}/R_{r\,DC}$
Y1-C	1.427–1.691	4.12×10^{-3}	4.46×10^{-3}	0.923
Y2-C	1.120–1.780	4.95×10^{-3}	4.09×10^{-3}	1.210
Y3-C	0.894–1.712	4.92×10^{-3}	5.57×10^{-3}	0.884
Y6-C	1.349–1.570	4.47×10^{-3}	5.55×10^{-3}	0.805
Y8-C	1.182–1.395	6.16×10^{-3}	1.48×10^{-2}	0.417

Hence, this characteristic may imply the correlation between the pore distribution in 2D spaces and 3D spaces to some extent.

For sample Y8-C, the R_r predicted by the digital core is more than twice as much as the prediction of Eq. (5). The comparability for R_r deduced by these two methods for sample Y8-C weakens, which may be attributed to the following reasons. (1) As displayed in Fig. 11(b). The data distribution is significantly more concentrated for Y8-C compared to other samples. The clustering effect could compromise the fitting accuracy of parameter $R_{r\,EQ}$. (2) Essentially, the $R_{r\,EQ}$ and $R_{r\,DC}$ are both the ratio of the equivalent pore diameter of R_{min} and R_{max}. In this paper, the pore shapes in 2D and 3D spaces are assumed to be round and spherical, respectively. However, as illustrated in Fig. 7(c3), the pore shape of the maximum pore for sample Y8-C is a sheet-like geometry rather than spherical, while this pore is treated as spherical when calculating $R_{r\,EQ}$. The discrepancy between actual and assumed pore shapes directly introduces inaccuracies for the prediction of R_r, particularly when significant differences exist between the actual pore shape and the hypothetical pore geometry used for analysis. Therefore, the hypothetical pore shape should be carefully considered when analyzing the pores in digital cores.

In 3D space, the fractal dimensions for sandstones in YL UGS are distributed between 2 and 3 (Fig. 12). Different from the 2D fractal dimensions for each slice, the $D_{f\,3D}$ is the overall description of the complexity of pore distribution of 3D digital core. On the other hand, similar to the findings of 2D space analysis, the pore distribution in 3D space in the core zone shows stronger complexity and higher occupancy, whereas the pores in the periphery zone exhibit lower complexity and occupancy. The consistency in the pore complexity assessment by fractal dimensions further corroborates the correlation of microstructure in 2D and 3D spaces. Firstly, the scaling law is also satisfied in 3D space for the

sandstones in YL UGS. Secondly, the predictions for R_r by equation analysis and digital core analysis are consistent. According to the fitting results illustrated in Fig. 12, the $R_{r\ EQ}$ in 3D space for these samples is 2.42×10^{-3}, deducing an R_{max} in 3D space of 384.56 μm, which indicates the pores across two ends of the digital core with a physical size of 768^3 μm^3 in some extreme cases. Analyzing 2D slices, the size of a typical pore can reach 777.67 μm, whose radius is interestingly similar to the $R_{r\ EQ}$ predicted above. Therefore, the consistency between pore spatial analyses conducted at different dimensional levels is reinforced.

4.4.2. Lacunarity and heterogeneity of pores

In section 4.3, it has been found that there are distinct differences in pore size distributions across various samples, indicating the heterogeneity of storage spaces in YL UGS. This heterogeneity can be qualitatively identified by analyzing Figs. 7 and 9. Specifically, larger pores are densely distributed in core zone sample (Y1-C), while smaller pores are more dispersedly distributed in the periphery zone sample (Y8-C).

To achieve a quantitative assessment of pore aggregation heterogeneity across different zones of YL UGS, the normalized lacunarity at various sizes of gliding boxes is calculated (Fig. 13). $\Lambda^*(r)$ is distributed between 0 and 1, and $\Lambda^*(r=1)$ and $\Lambda^*(r=512)$ are its upper and lower bounds, respectively. Notably, the $\Lambda^*(r)$ values at the same r always decrease from sample Y1-C to Y3-C and Y8-C, except for the upper and lower bounds of the normalized lacunarity spectrum. The comparative analysis of $\Lambda^*(r)$ values for these specific samples reveals that the core zone exhibits the strongest aggregation heterogeneity of pore, followed by the transition zone, and the periphery zone exhibits the weakest pore aggregation, which is consistent with Fig. 7.

From a microscopic perspective, the stronger pore aggregation degree suggests the pores may be easier to form connected pore spaces, which is advantageous for gas flow. The permeability for these three samples is 2.10, 0.04, and 0.03 mD, respectively, which decreasing trend is the same as $\Lambda^*(r)$. Hence, the inference on pore aggregation degree-gas flow capacity correlation is then confirmed to some extent.

4.4.3. Succolarity and connectivity of pores

The connectivity of pores is another important microstructural parameter, which not only affects the effective storage spaces in

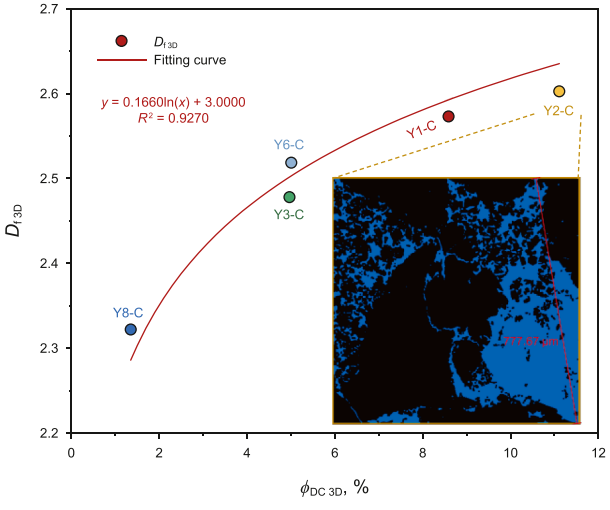

Fig. 12. Porosity versus fractal dimension for the sandstone digital cores in different zones of YL UGS.

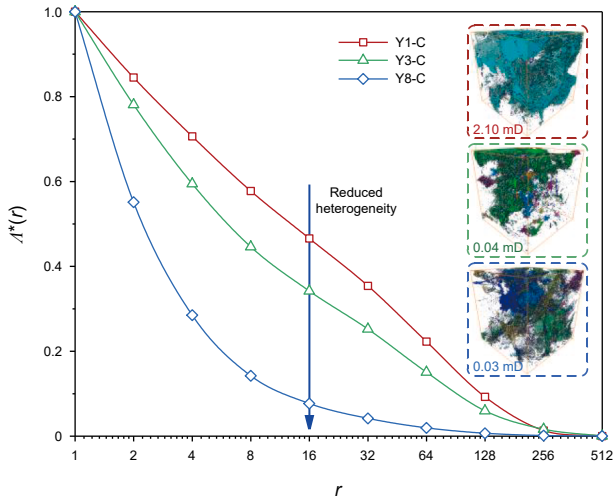

Fig. 13. Lacunarity for the sandstones in different zones of YL UGS.

UGS but also determines the gas flow capacity. To analyze the pore connectivity within different zones of YL UGS, the connected pores in different directions of digital cores are extracted, and their succolarity values are also calculated (Fig. 14). The core zone sample Y1-C possesses the strongest pore connectivity among the three samples, with an average of 97.17% connected pores. While that value decreases to 57.20% for the transition zone sample Y3-C, and the periphery zone sample Y8-C only owns 18.80% of connected pores on average. Furthermore, the analysis from the fractal geometry perspective also demonstrates the significant discrepancy in pore connectivity. The succolarity values for these three samples range from 5.72×10^{-2}–1.10×10^{-1}, 1.06×10^{-5}–5.12×10^{-2}, and 3.59×10^{-4}–1.62×10^{-3}, with average values of 8.34×10^{-2}, 2.31×10^{-2}, and 1.10×10^{-3}, respectively. These results further confirm that pore connectivity is decreasing from the core zone to the transition and periphery zones. Generally, strong connectivity in the core zone can constitute an effective pore network for fluid storage and flow, which has a positive impact on gas flow capacity. Good connectivity is also one of the important reasons why the core zone has the highest permeability among zones (Table 1 and Fig. 6(b)).

In addition to overall cognitions in pore connectivity, directional variation in pore connectivity, i.e., anisotropy, is also an important microstructural parameter. Anisotropy analysis is critical not only for identifying dominant flow directions but also for guiding engineering schemes related to UGS, such as optimizing the design of injection-production wells and determining reservoir reconstruction strategies. By analyzing the digital cores of connected pores (quantity and geometry) and their succolarity values in different directions, the anisotropy of pore connectivity can be preliminarily explored. For core zone sample Y1-C, the pores are all well-connected regardless of direction, with slight discrepancies in succolarity values (Fig. 14). It indicates that this sample represents relatively weak anisotropy. In contrast, the transition zone sample Y3-C exhibits higher anisotropy. While the quantity and distribution of connected pores are similar across directions, significant differences in the pore distributions appear in specific directions (e.g., Bm-T and Be-F). In addition, the succolarity in different directions of sample Y3-C shows a large discrepancy, also implying relatively stronger anisotropy to some extent compared to Y1-C. According to the digital cores in Fig. 14, the differences in the connected pore distribution of sample Y8-C get greater. A portion of connected pores in three directions (Bm-T, Be-F, and R-L) are

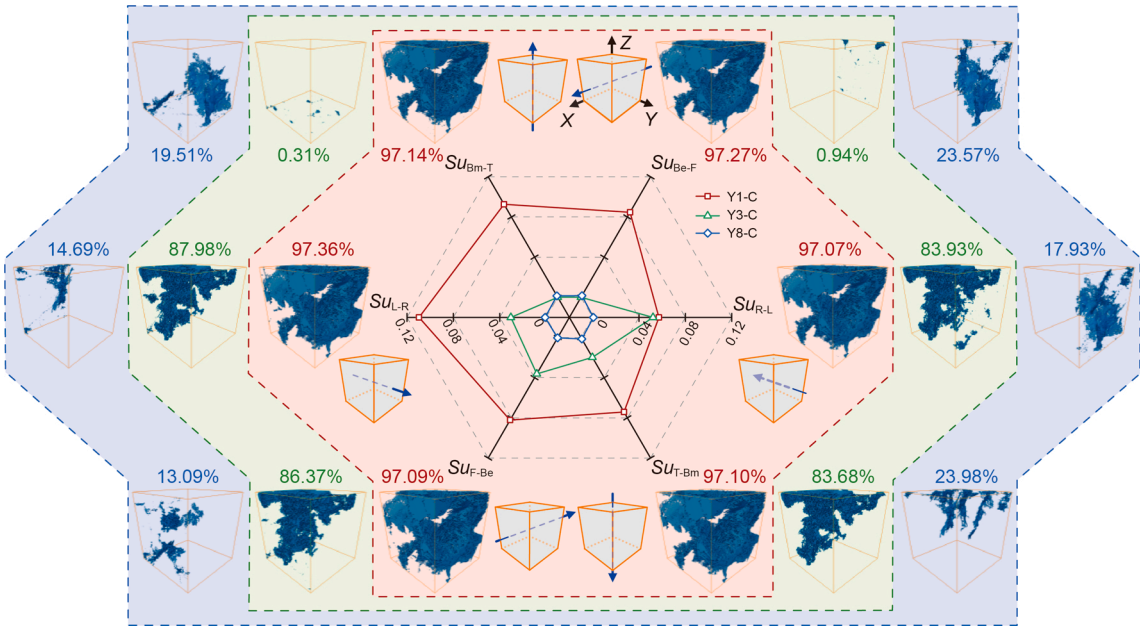

Fig. 14. Succolarity and connected pores for the sandstones in different zones of YL UGS. Subscripts L-R, R-L, Bm-T, T-Bm, Be-F, and F-Be represent different directions. Numbers next to the digital cores are the ratios of connected pores in different directions. *P* values for the succolarity of three samples are less than 0.026.

similar, while the other three directions have quite different connected pores, implying the highest anisotropy within the three samples. However, succolarity values cannot fully capture this level of anisotropy for Y8-C because the succolarity values in different directions are very small and show minimal differences. Moreover, the characteristics of weak connectivity and low succolarity of Y8-C also reflect its poor permeability to some extent.

Theoretically, succolarity is a measure of relative strength in pore connectivity in different directions. In most cases, succolarity alone is insufficient to determine the degree of anisotropy (such as Y1-C and Y8-C). In some specific cases, a relatively stronger anisotropy in pore connectivity can be identified, especially when directional variations of succolarity are intense (such as Y3-C). After a qualitative judgment on anisotropy is made, succolarity can then be used as a kind of supplement or verification to the results. Therefore, succolarity can serve as one component of the comprehensive analysis of pore connectivity strength and directional variation.

5. Discussion

5.1. Controlling factors of gas storage capacity

5.1.1. Effects of mineral compositions

Porosity of cylindrical samples is a direct measure of storage capacity for a UGS. As shown in Fig. 15, the porosity of sandstones appears to be significantly controlled by their mineral compositions. Sandstones with higher quartz contents and lower clay mineral contents generally exhibit better storage performance. Essentially, the void spaces within porous media that are not occupied by solid components are pores, i.e., the storage spaces for sandstone herein. In terms of mineralogical characteristics of sandstone, on one hand, a mass of larger-sized and rigid quartz grains is favorable to forming more primary intergranular pores during its deposition and also possesses fair performance to resist the compaction-induced reduction of pore spaces. On the other hand, the presence of large amounts of clay may be disadvantageous for the storage capacity of sandstones, since the smaller-sized clay tends to fill the interparticle pores created by quartz grains during deposition. Additionally, clay aggregations have weaker resistance against compaction, leading to further reductions in pore spaces and pore sizes. Taking these theoretical considerations into account, sandstone with a higher quartz content is more prone to develop more pore spaces, while that is opposite for a higher clay mineral content. That is the microscopic explanation of composition-controlled storage capacity for sandstones within YL UGS.

5.1.2. Effects of sandstone microstructures

Compared to standard cylindrical cores, the porosity of digital cores is also an important indicator for storage capacity assessment at a more microscopic scale. Herein, the intercorrelations of petrophysical and microstructural parameters for 5 CT-scanned sandstones within YL UGS are analyzed, and the results are shown in Fig. 16. Among these parameters, porosity and permeability are usually regarded as measures of petrophysical properties, while the other parameters are mainly the representation of microstructural characteristics. Similar to the cylindrical cores illustrated in Fig. 5, there is a positive correlation between porosity of digital cores and permeability ($R = 0.89$).

At a microscopic scale, the porosity of digital cores is strongly positively correlated to multiple microstructural parameters. Based on their Pearson correlation coefficients in Fig. 16, these parameters are ranked in descending order of Λ^*, Su_{avg}, $D_{f\,3D}$, $T_{avg\ PNM}$, $L_{avg\ PNM}$, $R_{avg\ DC}$, $R_{avg\ PNM}$, and variance of pore distribution. The results show that the heterogeneity, connectivity, and complexity of pores are the most influential microstructural parameters for the storage capacity of these sandstones, followed by the throat geometry and average pore size. This phenomenon also validates the applicability of fractal parameters in microstructure characterization for sandstones, as they demonstrate strong statistical relationships with not only storage capacity, but also with permeability and multiple microstructural properties. Notably, a weak positive relationship between porosity of digital cores and average coordination number is observed. The average coordination number ranges from 4.41 to 7.10, demonstrating relatively favorable pore connectivity at the pore scale for all 5 sandstones. However, this kind of assessment of connectivity is

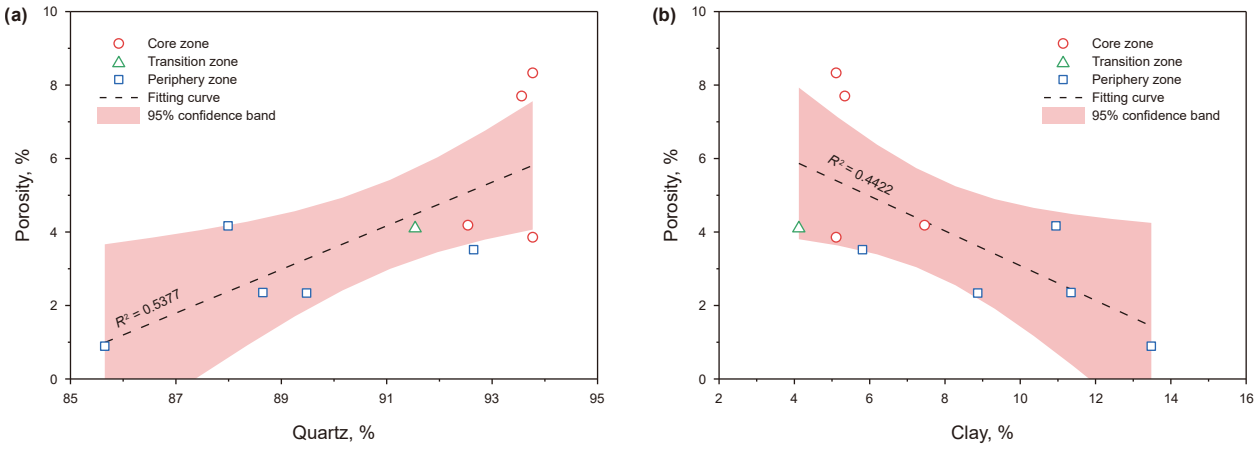

Fig. 15. Correlations between porosity and **(a)** quartz content and **(b)** clay content of sandstones in YL UGS. Where porosity is the test result of gravimetric method on cylindrical samples.

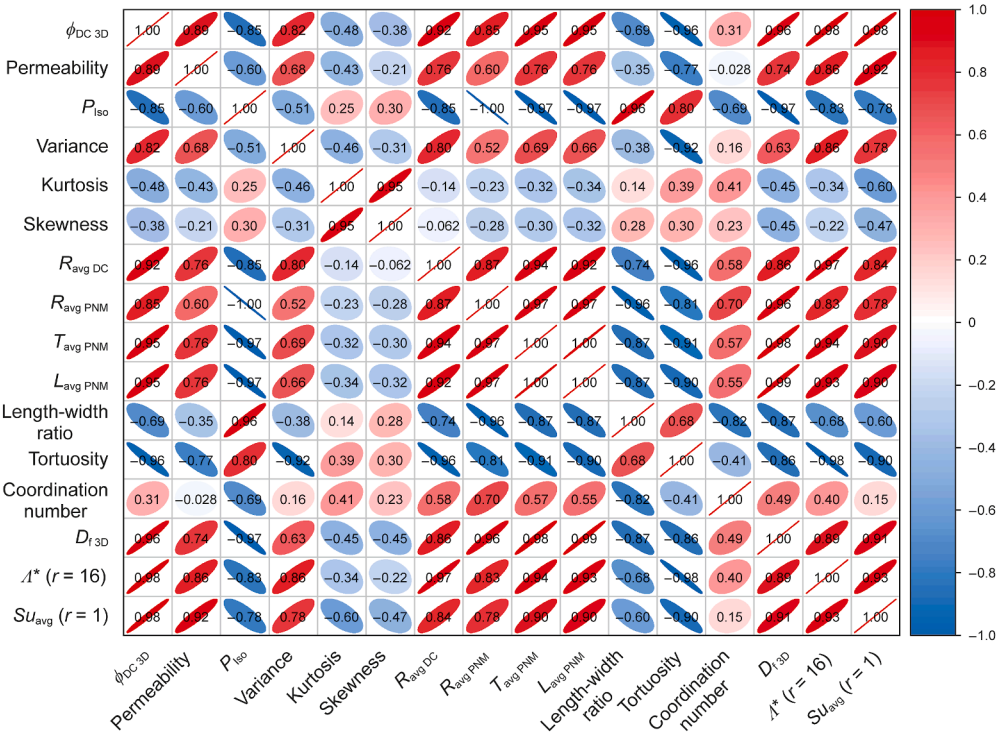

Fig. 16. Correlations of petrophysical and microstructural parameters. P_{Iso} is proportion of isolated pores; $R_{avg\ DC}$ is the average pore radius of digital core; $R_{avg\ PNM}$ is the average pore radius of PNM model; $T_{avg\ PNM}$ is the average throat radius of PNM model; $L_{avg\ PNM}$ is average throat length of PNM model; Su_{avg} is the average of succolarity in six directions. Numbers in the heat map are Pearson correlation coefficients R. $|R| \geq 0.8$ indicates a strong correlation, $0.4 \leq |R| < 0.8$ shows a medium correlation, and $0.4 < |R|$ is considered to be weak or no correlation.

invalid at the scale of the digital core, since it contradicts the cognition on pore connectivity illustrated in Fig. 14. Therefore, the average coordination number cannot tell the microstructural difference for the studied samples accurately. In this study, compared with the average coordination number, the fractal parameter succolarity is more applicable for pore connectivity representation.

Furthermore, some microstructural parameters exhibit negative correlations with storage capacity of sandstones, such as tortuosity, P_{Iso}, length-width ratio, and kurtosis pore distribution. These results suggest that sandstones with lower porosity tend to develop more tortuous and narrow pores, which is consistent with the theoretical analysis of pore evolution in subsection 5.1.1.

5.2. Feasibility analysis of UGS construction

In this section, the feasibility of UGS construction from large-scale low-permeability lithologic gas reservoirs is discussed. To give full play to the petrophysical advantages of each zone, several zone-differentiated engineering suggestions for UGS construction are proposed.

5.2.1. Simplified injection-production response

To preliminarily verify the feasibility of UGS construction in a large-scale low-permeability lithologic gas reservoir, a simple single-well injection-production numerical simulation is conducted using the tNavigator software (version 24.1). The

Table 3
Parameter settings for single-well injection-production numerical simulation.

Parameters	Values
Reservoir burial depth, m	2945–2955
Reservoir temperature, °C	90
Initial reservoir pressure in the simulation, MPa	14
Radius of core zone, m	2000
Area proportion of core zone	0.28
Area proportion of transition zone	0.17
Area proportion of periphery zone	0.55
Grid size, m × m × m	50 × 50 × 0.5
Porosity, %	4.78/3.09/2.75
Permeability in *x*/*y*-direction, mD	1.3/0.4
Permeability in *z*-direction, mD	0.13/0.04
Inner diameter of the well, m	0.1
Skin factor	−1
Time step, d	7
Duration of injection, d	212
Bottom hole pressure during injection, MPa	30
Duration of production, d	135
Bottom hole pressure during production, MPa	5

parameter settings are shown in Table 3 and Fig. 17. The petrophysical properties fully consider the results of this study (Fig. 6), and the other parameters refer to the general characteristics of the YL block.

The results of the single-well injection-production numerical simulation are shown in Fig. 18. During the 212-day injection period, the daily gas injection of the straight well W1 ranges from (16.8–13.5) × 10^4 m^3, with an average of 14.3 × 10^4 m^3 (Fig. 18(a)). After gas injection, the formation pressure around the well rises significantly, while the pressure at a distance of 1116 m from the injection-production well only increases by 0.5 MPa (Fig. 18(c)). For the gas production stage, the daily gas injection production ranges from (9.9–6.1) × 10^4 m^3, with an average of 7.0 × 10^4 m^3 (Fig. 18(b)). The pressure spread range after gas production is 427 m (Fig. 18(d)). It indicates that the gas spread range within the core zone is relatively limited under this gas injection and production condition, further verifying the rationality of the "three zones" collaborative construction mode. In future work, more complex and systematic numerical simulation studies should be conducted on actual UGS to demonstrate its gas injection-production capacity and the effectiveness of dynamic boundaries.

5.2.2. Zone functions and engineering suggestions

5.2.2.1. Overview of three zones. In summary, there is a significant zonal heterogeneity in the microscopic storage spaces of a large-scale low-permeability lithologic gas reservoir (Fig. 19). The core zone is characterized by higher porosity and permeability, pore aggregation degree, pore connectivity, spatial complexity, pore and throat size, and quartz content; while the pore tortuosity, ratio of isolated pores, length-width ratio, and clay mineral content are relatively low. The situation is the opposite for the transition and periphery zones. From core zone to transition and periphery zones, the petrophysical and microstructural properties get worse successively. For a more reasonable engineering decision and design of UGS, the importance matrix of different zones is provided, as shown in Table 4.

5.2.2.2. Core zone. The core zone possesses the highest storage capacity (Fig. 6(a)), flow capacity (Fig. 6(b)), and gas productivity (Fig. 1), which satisfies the positioning of the gas injection and production areas in the "three zones" collaborative construction mode of UGS (Table 4). The reason is that the property of microscopic storage spaces in the core zone is superior (Fig. 19). Specifically, the larger amount, larger-sized and more straight pores form a more aggregated and less anisotropic connected pore networks, which meet the necessary condition for large-scale underground storage and extraction of gases, such as natural gas, carbon dioxide, and hydrogen, etc. Even so, the nature of low-permeability and limited reservoir thickness of some lithologic gas reservoirs still limits gas injection and production capacity severely. Therefore, it is suggested to deploy an appropriate number of injection-production wells (mainly horizontal wells, supplemented by directional wells and straight wells) to fully utilize the storage capacity in the core zone and ensure economic benefits (Fig. 19). Fractal analysis reveals that the microscopic storage spaces in the core zone show higher aggregation and lower anisotropy. Hence, the direction of the horizontal section of the horizontal well is mainly determined by reservoir distribution (i.e., planar distribution and vertical thickness). To arrange the wells more reasonably, it is necessary to carry out multi-cycle injection-production numerical simulations. Based on the results of numerical simulation, the number of injection-production wells and the well deployment scheme can then be optimized. Gentle reservoir reconstruction technologies, such as moderate acidification, are also suggested to further enhance the injection and production capacity of gas wells.

5.2.2.3. Transition and periphery zones. The transition and periphery zones are characterized by poorer storage and flow capacities (Fig. 6), moderate to poor production capacity (Fig. 1), and stronger anisotropy (Fig. 14), which makes it uneconomic to

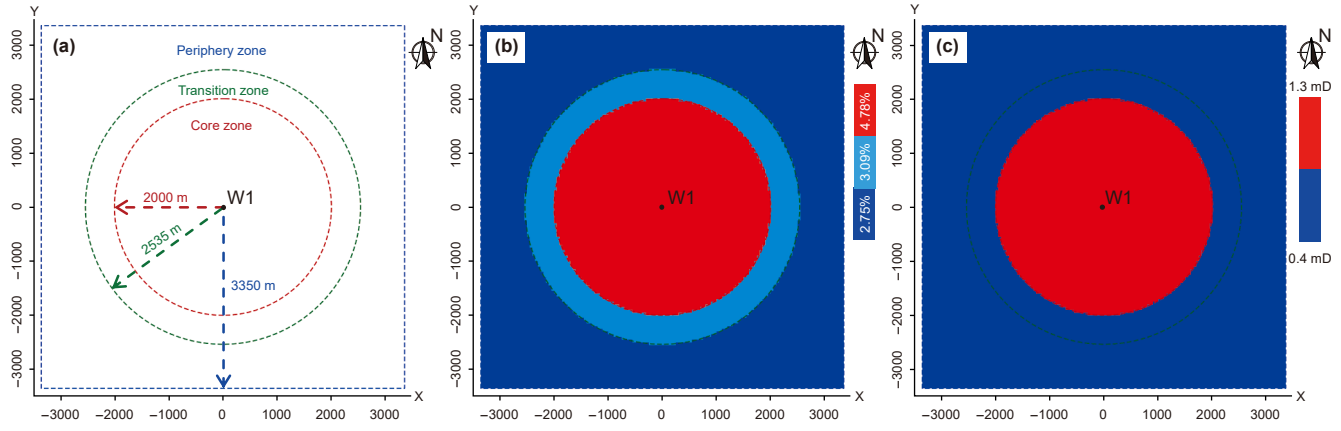

Fig. 17. **(a)** Geometric, **(b)** porosity, and **(c)** permeability settings of the numerical simulation model.

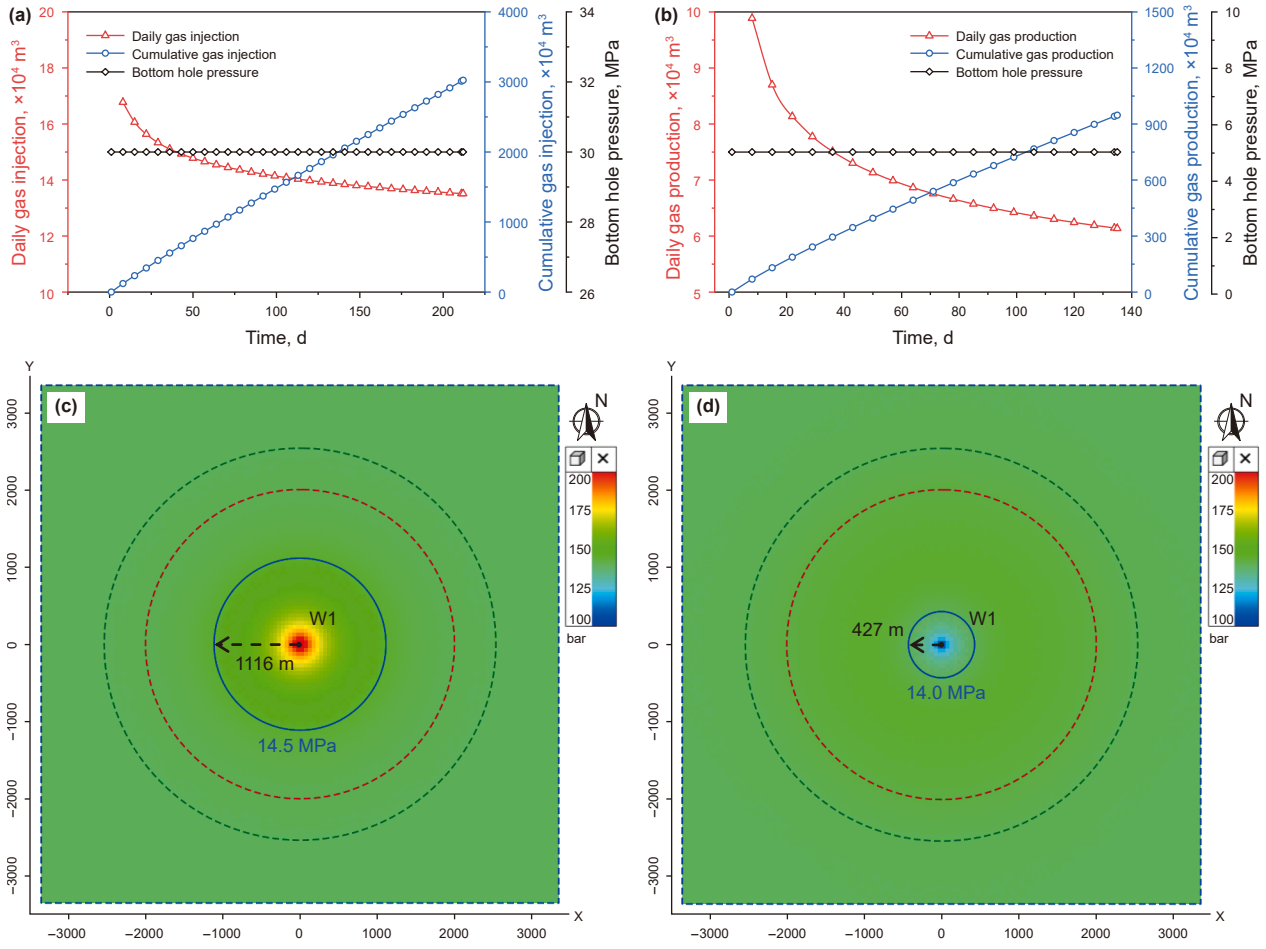

Fig. 18. **(a)** Gas injection and **(b)** gas production capacity of a single well, pressure response **(c)** at the end of the gas injection period and **(d)** at the end of the gas production period.

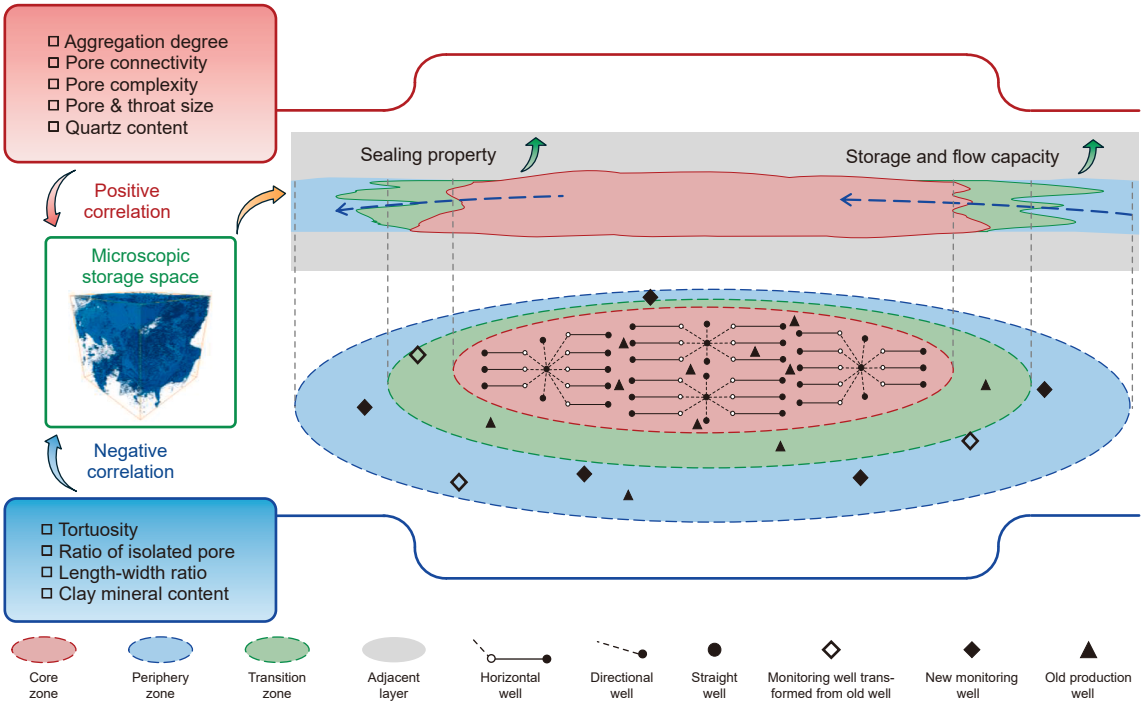

Fig. 19. Microstructural characteristics of different zones and the construction schematic diagram of UGS from a large-scale low-permeability lithologic gas reservoir.

Table 4
Engineering roles and the importance of different zones for UGS construction.

Engineering roles	Core zone	Transition zone	Periphery zone
Storage capacity	***	**	*
Injectivity	***	*	*
Productivity	***	*	*
Lateral sealing capacity	*	**	***
Leakage risk	*** (vertical)	*** (lateral)	**
Operational complexity	***	*	*
Monitoring requirements	***	***	**

Note: symbol "***" means very important, symbol "**" means important, symbol "*" means less important.

deploy injection-production wells (Fig. 19 and Table 4). However, due to their poorer petrophysical and microstructural properties (lower permeability, pore size, connectivity, and tortuosity), the transition and periphery zones are natural lateral barriers of the core zone. On the other hand, due to its adjacency to the core zone, the transition zone will inevitably respond to the injection and production activities in the core zone. Therefore, the transition zone may passively provide the collaborative gas injection-production function with the core zone. Overall, the transition and periphery zones are suggested to provide the functions of reservoir monitoring and integrity evaluation (Table 4), which is in line with the "three zones" collaborative construction mode. The specific approach is to detect reservoir pressure, microearthquake, and microgravity in these areas by old production wells that can be reutilized, if necessary, deploy new monitoring wells (Fig. 19). The monitoring data are also available for the assessments of gas storage capacity and leakage amount of UGS, further determining the reasonable operational scheme for the injection-production wells in the core zone in different injection-production cycles. Regarding the disposal of old wells, seal the old production wells that cannot be reutilized at a proper time to ensure the integrity of the UGS. It should be noted that the sealing of these old production wells is not the earlier the better. On the premise of ensuring the integrity of the UGS, old production wells should be utilized as much as possible to monitor the formation pressure, to deepen the understanding of the connectivity of the reservoir, and to provide feasible adjustment suggestions for the construction of UGS.

6. Conclusions

(1) Micro-CT and PNM analysis reveal the storage spaces having a decreased total pore space, connected pore ratio, average pore and throat size, and an increased length-width ratio and tortuosity of pores from core zone to transition zone and periphery zone. In addition, the core zone shows a wider distribution range of pore volume, pore radius, throat radius, and throat length.

(2) Fractal geometry analysis represents a decreased fractal dimension, lacunarity, and succolarity of the storage spaces from core zone to transition zone and periphery zone, indicating a stronger spatial occupancy, aggregation degree, and pore connectivity in the core zone.

(3) Mineral compositions and microstructures are important controlling factors of gas storage spaces of sandstones within YL UGS. A higher gas storage capacity is usually positively related to pore heterogeneity, pore connectivity, pore complexity, throat and pore size, and quartz content, while it is negatively related to pore tortuosity, proportion of isolated pores, length-width ratio of pore, variance of pore distribution, and clay mineral content.

(4) Core zone is the main injection-production region of the large-scale low-permeability lithologic gas reservoir-type UGS. Reasonable well patterns and reconstruction technologies are the guarantee of storage and supply capacity of natural gas. Transition and periphery zones show poorer storage capacity, which can be used for the integrity monitoring and gas leakage assessment of UGS.

These findings deepen our understanding of microscopic storage spaces and their heterogeneity in large-scale low-permeability lithologic gas reservoirs, and preliminarily verify the feasibility of UGS construction from this type of gas reservoir. Different from the overall construction mode of structural gas reservoirs, this cognition supports a zone-differentiated construction mode of UGS, which is of great significance for breaking through the engineering challenge of UGS construction from large-scale low-permeability lithologic gas reservoirs.

CRediT authorship contribution statement

Zhen-Hua Tian: Writing – original draft, Software, Methodology, Conceptualization. **Yong Xia:** Writing – original draft, Project administration, Funding acquisition, Conceptualization. **Jian-Guo Zhang:** Writing – review & editing, Investigation. **De-Long Wang:** Visualization, Formal analysis. **Zhi-Jun Liu:** Validation, Supervision. **Chen-Yang Zhao:** Methodology, Validation. **Yu-Xuan Xia:** Writing – review & editing, Software, Funding acquisition. **Jun-Wei Su:** Writing – review & editing. **Deng-Ke Liu:** Writing – review & editing, Data curation. **Jian-Chao Cai:** Writing – review & editing, Supervision, Methodology.

Declaration of competing interest

The authors declare that they have no known competing financial interests or personal relationships that could have appeared to influence the work reported in this paper.

Acknowledgments

The authors are grateful for the support of the Research on Key Technologies for Efficient Construction and Safe Operation of Underground Gas Storage (No. 2023YQX106) and the National Natural Science Foundation of China (No. 42302143).

References

Adebayo, T.S., Kartal, M.T., Ullah, S., 2023. Role of hydroelectricity and natural gas consumption on environmental sustainability in the United States: evidence from novel time-frequency approaches. J. Environ. Manag. 328, 116987. https://doi.org/10.1016/j.jenvman.2022.116987.

Allain, C., Cloitre, M., 1991. Characterizing the lacunarity of random and deterministic fractal sets. Phys. Rev. A 44 (6), 3552–3558. https://doi.org/10.1103/PhysRevA.44.3552.

Al-Shafi, M., Massarweh, O., Abushaikha, A.S., et al., 2023. A review on underground gas storage systems: natural gas, hydrogen and carbon sequestration. Energy Rep. 9, 6251–6266. https://doi.org/10.1016/j.egyr.2023.05.236.

Anovitz, L.M., Cole, D.R., 2015. Characterization and analysis of porosity and pore structures. Rev. Mineral. Geochem. 80 (1), 61–164. https://doi.org/10.2138/rmg.2015.80.04.

Arif, M., Mahmoud, M., Zhang, Y., et al., 2021. X-ray tomography imaging of shale microstructures: a review in the context of multiscale correlative imaging. Int. J. Coal Geol. 233, 103641. https://doi.org/10.1016/j.coal.2020.103641.

Bahrami, M., Mahani, H., Zivar, D., et al., 2024. Microfluidic investigation of pore-scale flow behavior and hysteresis in underground hydrogen storage in sandstones. J. Energy Storage 98, 112959. https://doi.org/10.1016/j.est.2024.112959.

Bai, M., Shen, A., Meng, L., et al., 2018. Well completion issues for underground gas storage in oil and gas reservoirs in China. J. Pet. Sci. Eng. 171, 584–591. https://doi.org/10.1016/j.petrol.2018.07.061.

Ban, S., Liu, H., Wei, X., et al., 2023. The application of the fuzzy comprehensive evaluation method in the sealing evaluation of caprocks in underground gas storage. Appl. Sci.-Basel 13 (17), 9753. https://doi.org/10.3390/app13179753.

Blunt, M.J., Sun, S., Boone, M.A., et al., 2025. Digital rock physics and fluid flow in the context of the energy transition. Adv. Geo-Energy Res. 18 (3), 299–302. https://doi.org/10.46690/ager.2025.12.10.

Bugaje, A.-A.B., Dioha, M.O., Abraham-Dukuma, M.C., et al., 2022. Rethinking the position of natural gas in a low-carbon energy transition. Energy Res. Social Sci. 90, 102604. https://doi.org/10.1016/j.erss.2022.102604.

Bushell, G.C., Yan, Y.D., Woodfield, D., et al., 2002. On techniques for the measurement of the mass fractal dimension of aggregates. Adv. Colloid Interface Sci. 95 (1), 1–50. https://doi.org/10.1016/S0001-8686(00)00078-6.

Cai, J., Hu, X., 2015. Fractal Theory in Porous Media and its Applications. Science Press, Beijing.

Cai, J., Tian, Z., Zhou, S., et al., 2024. A critical mini-review of key issues on sweet spot identification for shale gas reservoirs. Energy Rev. 3 (4), 100101. https://doi.org/10.1016/j.enrev.2024.100101.

CEDIGAZ, 2024. Underground Gas Storage: Pillar of Global Energy Security. Available from: https://www.cedigaz.org/underground-gas-storage-pillar-of-global-energy-security/. (Accessed 30 June 2025).

Cnudde, V., Boone, M.N., 2013. High-resolution X-ray computed tomography in geosciences: a review of the current technology and applications. Earth-Sci. Rev. 123, 1–17. https://doi.org/10.1016/j.earscirev.2013.04.003.

Datseris, G., Kottlarz, I., Braun, A.P., et al., 2023. Estimating fractal dimensions: a comparative review and open source implementations. Chaos 33 (10), 102101. https://doi.org/10.1063/5.0160394.

de Melo, R.H.C., Conci, A., 2013. How succolarity could be used as another fractal measure in image analysis. Telecommun. Syst. 52 (3), 1643–1655. https://doi.org/10.1007/s11235-011-9657-3.

Ding, G., Liu, H., Xia, D., et al., 2023. Experimental study of the shear characteristics of fault filled with different types of gouge in underground gas storage. Energies 16 (7), 3119. https://doi.org/10.3390/en16073119.

Dong, K., Jiang, Q., Shahbaz, M., et al., 2021. Does low-carbon energy transition mitigate energy poverty? The case of natural gas for China. Energy Econ. 99, 105324. https://doi.org/10.1016/j.eneco.2021.105324.

Du, J., Li, X., Bao, H., et al., 2019. Geological conditions of natural gas accumulation and new exploration areas in the Mesoproterozoic to lower Paleozoic of Ordos Basin, NW China. Petrol. Explor. Dev. 46 (5), 866–882. https://doi.org/10.1016/S1876-3804(19)60246-6.

Fan, J., Wang, J., Liu, M., et al., 2022. Scenario simulations of China's natural gas consumption under the dual-carbon target. Energy 252, 124106. https://doi.org/10.1016/j.energy.2022.124106.

Feder, J., 1988. Fractals. Plenum Press, New York.

Garum, M., Glover, P.W.J., Lorinczi, P., et al., 2020. Micro- and nano-scale pore structure in gas shale using Xμ-CT and FIB-SEM techniques. Energy Fuels 34 (10), 12340–12353. https://doi.org/10.1021/acs.energyfuels.0c02025.

He, J., Yu, H., He, G., et al., 2022. Natural gas development prospect in Changqing gas province of the Ordos Basin. Nat. Gas. Ind. B 9 (2), 197–208. https://doi.org/10.1016/j.ngib.2021.08.023.

Guo, J.C., Zhou, H.Y., Zeng, J., et al., 2020. Advances in low-field nuclear magnetic resonance (NMR) technologies applied for characterization of pore space inside rocks: a critical review. Pet. Sci. 17 (5), 1281–1297. https://doi.org/10.1007/s12182-020-00488-0.

He, Y., Xie, Y., Qiao, Y., et al., 2024. Estimation of underground hydrogen storage capacity in depleted gas reservoirs using CO_2 as cushion gas. Appl. Energy 375, 124093. https://doi.org/10.1016/j.apenergy.2024.124093.

Ji, W., Wan, J., Li, J., et al., 2024. Integration of large-scale underground energy storage technologies and renewable energy sources. Adv. Geo-Energy Res. 14 (2), 81–85. https://doi.org/10.46690/ager.2024.11.01.

Jiang, F., Chen, D., Chen, J., et al., 2016. Fractal analysis of shale pore structure of continental gas shale reservoir in the Ordos Basin, NW China. Energy Fuels 30 (6), 4676–4689. https://doi.org/10.1021/acs.energyfuels.6b00574.

Jiang, F., Huo, L., Chen, D., et al., 2023. The controlling factors and prediction model of pore structure in global shale sediments based on random forest machine learning. Earth-Sci. Rev. 241, 104442. https://doi.org/10.1016/j.earscirev.2023.104442.

Kushnir, R., Ullmann, A., Dayan, A., 2012. Thermodynamic and hydrodynamic response of compressed air energy storage reservoirs: a review. Rev. Chem. Eng. 28 (2–3), 123–148. https://doi.org/10.1515/revce-2012-0006.

Lai, J., Wang, G., Wang, Z., et al., 2018. A review on pore structure characterization in tight sandstones. Earth-Sci. Rev. 177, 436–457. https://doi.org/10.1016/j.earscirev.2017.12.003.

Li, Y., Gao, X., Meng, S., et al., 2019. Diagenetic sequences of continuously deposited tight sandstones in various environments: a case study from upper Paleozoic sandstones in the Linxing area, eastern Ordos basin, China. AAPG Bull. 103 (11), 2757–2783. https://doi.org/10.1306/03061918062.

Li, J., Xia, Y., Wang, D., et al., 2023. Key technologies of construction design and operation optimization for underground gas storage of low permeability lithologic gas reservoirs in Ordos Basin. Nat. Gas Geosci. 34 (8), 1442–1451 (in Chinese). http://www.nggs.ac.cn/EN/10.11764/j.issn.1672-1926.2023.03.005.

Liu, H., Yang, C., Liu, J., et al., 2023. An overview of underground energy storage in porous media and development in China. Gas Sci. Eng. 117, 205079. https://doi.org/10.1016/j.jgsce.2023.205079.

Liu, J., Yang, C., Song, R., et al., 2025. Advances of geological storage engineering and technology. GeoStorage 1 (1), 1–26. https://doi.org/10.46690/gs.2025.01.01.

Lyu, X., Wang, W., Voskov, D., et al., 2025. Multiscale modeling for multiphase flow and reactive mass transport in subsurface energy storage: a review. Adv. Geo-Energy Res. 15 (3), 245–260. https://doi.org/10.46690/ager.2025.03.07.

Ma, X., Zheng, D., Shen, R., et al., 2018. Key technologies and practice for gas field storage facility construction of complex geological conditions in China. Petrol. Explor. Dev. 45 (3), 507–520. https://doi.org/10.1016/S1876-3804(18)30056-9.

Mandelbrot, B.B., 1982. The Fractal Geometry of Nature. W. H. Freeman and Company, New York.

Matar, W., Shabaneh, R., 2020. Viability of seasonal natural gas storage in the Saudi energy system. Energy Strategy Rev. 32, 100549. https://doi.org/10.1016/j.esr.2020.100549.

Matos, C.R., Carneiro, J.F., Silva, P.P., 2019. Overview of large-scale underground energy storage technologies for integration of renewable energies and criteria for reservoir identification. J. Energy Storage 21, 241–258. https://doi.org/10.1016/j.est.2018.11.023.

Muhire, F., Turyareeba, D., Adaramola, M.S., et al., 2024. Drivers of green energy transition: a review. Green Energy Resour 2 (4), 100105. https://doi.org/10.1016/j.gerr.2024.100105.

Nayak, S.R., Mishra, J., Palai, G., 2019. Analysing roughness of surface through fractal dimension: a review. Image Vis. Comput. 89, 21–34. https://doi.org/10.1016/j.imavis.2019.06.015.

Qiao, J., Zeng, J., Cai, J., et al., 2021. Pore-scale heterogeneity of tight gas sandstone: origins and impacts. J. Nat. Gas Sci. Eng. 96, 104248. https://doi.org/10.1016/j.jngse.2021.104248.

Qiao, J., Zeng, J., Jiang, S., et al., 2020. Insights into the pore structure and implications for fluid flow capacity of tight gas sandstone: a case study in the upper paleozoic of the Ordos Basin. Mar. Petrol. Geol. 118, 104439. https://doi.org/10.1016/j.marpetgeo.2020.104439.

Roy, A., Perfect, E., Dunne, W.M., et al., 2010. Lacunarity analysis of fracture networks: evidence for scale-dependent clustering. J. Struct. Geol. 32 (10), 1444–1449. https://doi.org/10.1016/j.jsg.2010.08.010.

Saeed, M., Jadhawar, P., 2024. Modelling underground hydrogen storage: a state-of-the-art review of fundamental approaches and findings. Gas Sci. Eng. 121, 205196. https://doi.org/10.1016/j.jgsce.2023.205196.

Saif, T., Lin, Q., Butcher, A.R., et al., 2017. Multi-scale multi-dimensional microstructure imaging of oil shale pyrolysis using X-ray micro-tomography, automated ultra-high resolution SEM, MAPS Mineralogy and FIB-SEM. Appl. Energy 202, 628–647. https://doi.org/10.1016/j.apenergy.2017.05.039.

Sekar, L.K., Kiran, R., Okoroafor, E.R., et al., 2023. Review of reservoir challenges associated with subsurface hydrogen storage and recovery in depleted oil and gas reservoirs. J. Energy Storage 72, 108605. https://doi.org/10.1016/j.est.2023.108605.

Sendker, F.L., Lo, Y.K., Heimerl, T., et al., 2024. Emergence of fractal geometries in the evolution of a metabolic enzyme. Nature 628 (8009), 894–900. https://doi.org/10.1038/s41586-024-07287-2.

Singh, H., 2022. Hydrogen storage in inactive horizontal shale gas wells: Techno-economic analysis for Haynesville shale. Appl. Energy 313. https://doi.org/10.1016/j.apenergy.2022.118862.

Soroush, M., Alizadeh, N., 2008. Underground gas storage in a partially depleted gas reservoir. J. Can. Pet. Technol. 47 (2), 17–21. https://doi.org/10.2118/08-02-17-TN.

Teatini, P., Castelletto, N., Ferronato, M., et al., 2011. Geomechanical response to seasonal gas storage in depleted reservoirs: a case study in the Po River basin, Italy. J. Geophys. Res. Earth Surf. 116, F02002. https://doi.org/10.1029/2010JF001793.

Tian, Z., Wei, W., Zhou, S., et al., 2021. Experimental and fractal characterization of the microstructure of shales from Sichuan Basin, China. Energy Fuels 35 (5), 3899–3914. https://doi.org/10.1021/acs.energyfuels.0c04027.

Tian, Y., Yang, Y., Zhao, H., et al., 2025. Compositional simulation of coupled transport mechanisms in fractured-vuggy underground gas storage: a case study of LWC in the Sichuan Basin. Geoenergy Sci. Eng. 244, 213389. https://doi.org/10.1016/j.geoen.2024.213389.

Wang, J., Wang, J., Xu, S., et al., 2022. A novel mode for "three zones" collaborative reconstruction of underground gas storage and its application to large, low-permeability lithologic gas reservoirs. Energy 253, 124148. https://doi.org/10.1016/j.energy.2022.124148.

Wanyan, Q., Li, G., Zhu, H., et al., 2025. Major theories and key technologies of underground natural gas storage facilities in China: progress and prospects. Nat. Gas Geosci. 45 (1), 153–163. https://doi.org/10.3787/j.issn.1000-0976.2025.01.013 (in Chinese).

Wen, K., Lu, Y., Lu, M., et al., 2022. Multi-period optimal infrastructure planning of natural gas pipeline network system integrating flowrate allocation. Energy 257, 124745. https://doi.org/10.1016/j.energy.2022.124745.

Xia, Y., Cai, J., Perfect, E., et al., 2019. Fractal dimension, lacunarity and succolarity analyses on CT images of reservoir rocks for permeability prediction. J. Hydrol. 579, 124198. https://doi.org/10.1016/j.jhydrol.2019.124198.

Xia, Y., Zhang, J., He, Y., et al., 2023. Feasibility and operating index design of low permeability lithological reservoir into underground gas storage: case study of S area in Ordos Basin. Nat. Gas Geosci. 34 (8), 1452–1459. https://doi.org/10.11764/j.issn.1672-1926.2023.02.012 (in Chinese).

Xiao, L., Zhou, P., Bai, Y., et al., 2024. Modeling the dynamic allocation problem of multi-service storage system with strategy learning. Energy 302, 131597. https://doi.org/10.1016/j.energy.2024.131597.

Xie, J., Hao, X., Zhang, Y., et al., 2023a. Fracture identification and characteristics of carbonate underground gas storage: an example from the eastern area of Sulige gas field, Ordos Basin, China. Sci. Rep. 13 (1), 22446. https://doi.org/10.1038/s41598-023-50072-w.

Xie, Y., Wu, X., Hou, Z., et al., 2023b. Gleaning insights from German energy transition and large-scale underground energy storage for China's carbon neutrality. Int. J. Min. Sci. Technol. 33 (5), 529–553. https://doi.org/10.1016/j.ijmst.2023.04.001.

Yang, C., Wang, T., Chen, H., 2023. Theoretical and technological challenges of deep underground energy storage in China. Engineering 25, 168–181. https://doi.org/10.1016/j.eng.2022.06.021.

Yang, S., Hu, S., Qi, Z., et al., 2024. Experiment and prediction for dynamic storage capacity of underground gas storage rebuilt from hydrocarbon reservoir. Renew. Energy 222, 119908. https://doi.org/10.1016/j.renene.2023.119908.

Yu, B., Cheng, P., 2002. A fractal permeability model for bi-dispersed porous media. Int. J. Heat Mass Tran. 45 (14), 2983–2993. https://doi.org/10.1016/S0017-9310(02)00014-5.

Yu, B., Li, J., 2001. Some fractal characters of porous media. Fractals 9 (3), 365–372. https://doi.org/10.1142/s0218348x01000804.

Yuan, Y., Rezaee, R., 2019. Comparative porosity and pore structure assessment in shales: measurement techniques, influencing factors and implications for reservoir characterization. Energies 12 (11), 2094. https://doi.org/10.3390/en12112094.

Zhang, F., Tang, J., Zhou, J., et al., 2026a. Securing CO_2 storage in fractured reservoirs: intelligent characterization of critical natural fracture pathways. Fuel 406, 136915. https://doi.org/10.1016/j.fuel.2025.136915.

Zang, Q., Liu, C., Awan, R.S., et al., 2022. Occurrence characteristics of the movable fluid in heterogeneous sandstone reservoir based on fractal analysis of NMR data: a case study of the Chang 7 Member of Ansai Block, Ordos Basin, China. J. Pet. Sci. Eng. 214, 110499. https://doi.org/10.1016/j.petrol.2022.110499.

Zhang, J., Tan, Y., Zhang, T., et al., 2020. Natural gas market and underground gas storage development in China. J. Energy Storage 29, 101338. https://doi.org/10.1016/j.est.2020.101338.

Zhang, J., Xia, Y., Zhao, C., et al., 2023. Key technologies for geological evaluation of UGSs rebuilt from low-permeability lithological gas reservoirs in the Ordos Basin. Nat. Gas. Ind. 43 (10), 55–63. https://doi.org/10.3787/j.issn.1000-0976.2023.10.006 (in Chinese).

Zhang, M., Tang, J., Lv, W., et al., 2026b. Research on the storage performance evaluation and economic prediction of catalyzed green methanol underground. Appl. Energy 404, 126779. https://doi.org/10.1016/j.apenergy.2025.126779.

Zhao, P., He, B., Zhang, B., et al., 2022. Porosity of gas shale: is the NMR-based measurement reliable? Pet. Sci. 19 (2), 509–517. https://doi.org/10.1016/j.petsci.2021.12.013.

Zhao, Z., Cui, J., Liu, H., et al., 2024. Geo-mechanical evaluation of a proposed gas storage in aquifer anticline trap with deep fault. Bull. Eng. Geol. Environ. 83 (4), 102. https://doi.org/10.1007/s10064-024-03599-9.

Zheng, H., Yang, F., Guo, Q., et al., 2022. Multi-scale pore structure, pore network and pore connectivity of tight shale oil reservoir from Triassic Yanchang Formation, Ordos Basin. J. Pet. Sci. Eng. 212, 110283. https://doi.org/10.1016/j.petrol.2022.110283.

Zhou, S., Dong, D., Zhang, J., et al., 2021. Optimization of key parameters for porosity measurement of shale gas reservoirs. Nat. Gas. Ind. B 8 (5), 455–463. https://doi.org/10.1016/j.ngib.2021.08.004.

Zou, C., Li, S., Xiong, B., et al., 2024a. Revolution and significance of “Green Energy Transition” in the context of new quality productive forces: a discussion on theoretical understanding of “Energy Triangle”. Petrol. Explor. Dev. 51 (6), 1611–1627. https://doi.org/10.1016/S1876-3804(25)60564-7.

Zou, C., Lin, M., Ma, F., et al., 2024b. Development, challenges and strategies of natural gas industry under carbon neutral target in China. Petrol. Explor. Dev. 51 (2), 476–497. https://doi.org/10.1016/S1876-3804(24)60038-8.

Zou, C., Ma, F., Pan, S., et al., 2022. Earth energy evolution, human development and carbon neutral strategy. Petrol. Explor. Dev. 49 (2), 468–488. https://doi.org/10.1016/S1876-3804(22)60040-5.

Zou, C., Zhu, R., Liu, K., et al., 2012. Tight gas sandstone reservoirs in China: characteristics and recognition criteria. J. Pet. Sci. Eng. 88–89, 82–91. https://doi.org/10.1016/j.petrol.2012.02.001.